The steady-state flow pattern past gravitating bodies

C.W. Ormel[1]⋆†
[1] *Astronomy Department, University of California, Berkeley, CA 94720, USA*

21 February 2022

ABSTRACT

Gravitating bodies significantly alter the flow pattern (density and velocity) of the gas that attempts to stream past. Still, small protoplanets in the Mars–super-Earth range can only bind limited amounts of nebular gas; until the so-called critical core mass has been reached (∼1–10 Earth masses) this gas is in near hydrostatic equilibrium with the nebula. Here we aim for a general description of the flow pattern surrounding these low-mass, embedded planets. Using various simplifying assumptions (subsonic, 2D, inviscid flow, etc), we reduce the problem to a partial differential equation that we solve numerically as well as approximate analytically. It is found that the boundary between the atmosphere and the nebula gas strongly depends on the value of the disc headwind (deviation from Keplerian rotation). With increasing headwind the atmosphere decreases in size and also becomes more asymmetrical. Using the derived flow pattern for the gas, trajectories of small solid particles, which experience both gas drag and gravitational forces, are integrated numerically. Accretion rates for small particles (dust) are found to be low, as they closely follow the streamlines, which curl away from the planet. However, pebble-size particles achieve large accretion rates, in agreement with previous numerical and analytical works.

Key words: planets and satellites: formation – planetary systems: protoplanetary discs – hydrodynamics – methods: analytical

1 INTRODUCTION

Accretion of gas by gravitating objects is a common theme in astrophysics. The pioneering work in this field goes back the works of Hoyle & Lyttleton (1939) and Bondi & Hoyle (1944), who analytically derived the accretion rates for point-bodies (together known as Bondi-Hoyle-Lyttleton or BHL-accretion). Follow-up studies have refined these estimates, by considering the effects of the Mach number of the incident flow and the equation of state for the gas, mostly for supersonic flows (e.g., Hunt 1979; Shima et al. 1985; Ruffert 1995). In astrophysics, BHL-accretion plays a role in Binary systems, star- and galaxy formation, and the formation of gas-rich planets (e.g., Kley et al. 1995; Bonnell et al. 2001; Nelson & Benz 2003).

According to the core accretion model of planet formation, planets start out small and rocky as protoplanetary embryos (Mizuno 1980; Pollack et al. 1996; Weidenschilling 1997; Hubickyj et al. 2005). Once these embryos reach a size where their Bondi radius

$$R_b \equiv \frac{G_N M_p}{c_\infty^2} \qquad (1)$$

starts to exceed their physical radius R, they start to bind the gas from the nebula, forming a putative atmosphere. In equation (1) G_N is Newton's constant, M_p the mass of the perturber, and c_∞ the sound speed of the unperturbed system. As accreting planets are hotter than the background nebula – either from infalling solids (planetesimals) or from the residual heat of their formation (Ikoma & Hori 2012) – the resulting pressure gradient prevents contraction of the atmosphere. Therefore, the amount of gas these (small) bodies can acquire is initially limited: the protoplanet's atmosphere is in pressure-equilibrium with the surrounding nebular gas. [1] Small, hot protoplanets do not acquire gas akin to the BHL-regime: they must cool first.

However, at some critical core mass M_{crit} the steady state picture is no longer appropriate. Many detailed, 1D models have been developed to describe the quasi-static density structure of the protoplanet atmosphere and the crossover point (Stevenson 1982; Wuchterl 1993; Inaba & Ikoma 2003; Rafikov 2006). This crossover mass is often quoted as ∼10 $M_\oplus$ (Earth masses) but its precise value depends

---

⋆ E-mail: ormel@berkeley.edu
† Hubble Fellow

[1] Indeed, in a numerical experiment Terquem & Heinemann (2011) recently showed that, starting from a much condensed configuration, a protoplanet's atmosphere will expands and reconnect with the disc's gas to restore the near-hydrostatic state.

on detailed atmosphere models, and thereby on the equation of state, accretion luminosity, and opacities of gas and grains; it decreases to ~ 1 $M_\oplus$ for grain-free atmospheres (Hori & Ikoma 2010). Obviously, understanding the processes that determine $M_{\rm crit}$ is of key importance for planet formation; it may determine the transition between (super)-Earth/Neptune-like planets (bodies that have acquired limited amounts of gas) and gas giants (bodies that accrete gas in the BHL-regime).

In this work we will focus on the small planet regime, assuming a quasi-steady state. In a disc, the unperturbed gas flow, as seen from a frame rotating with the planet, consist of two components: a *shear* (due to the [Keplerian] rotation of the disc) and a systematic offset, which we refer to as the *headwind*. The latter arises from the slightly subkeplerian rotation of the gas, which is partially support by pressure. For a planet on a circular orbit, the value of the headwind is ηv_k with η (Adachi et al. 1976; Weidenschilling 1977):

$$\eta = \frac{1}{2\rho a \Omega^2}\frac{\partial P}{\partial a} = -\frac{1}{2}\frac{c_s^2}{v_K^2}\frac{\partial \ln P}{\partial \ln a} \sim \left(\frac{c_s}{v_k}\right)^2 \qquad (2)$$

where a, ρ, P, Ω, and v_K are the disc radius (semi-major axis), the corresponding gas density, pressure, orbital frequency, and orbital velocity. In this work the headwind is also defined in terms of a Mach number, $v_{\rm hw} = \mathcal{M}_{\rm hw}c_\infty$, i.e., $\mathcal{M}_{\rm hw} = \eta v_k/c_s \simeq \eta^{1/2}$. Only positive values of $v_{\rm hw}$ (a headwind; the gas rotates lower than Keplerian) are consider, but we remark that in special locations ('pressure bumps') $v_{\rm hw}$ may reverse sign. In addition, the flow, as seen in the frame of the planet, is subject to (noninertial) Coriolis forces and to the tidal force from the distant star. The flow pattern is therefore quite rich.

Understanding the flow pattern close to the planet is important for several reasons. For example, the flow pattern in the co-orbital region of the planet, where streamlines make a 'U-turn' (the horseshoe) is a critical ingredient for the co-orbital torque (Ward 1991; see also Paardekooper & Papaloizou 2009). Also, the location of the boundary between the nebular gas and the protoplanet's atmosphere is a parameter that affects the thermal evolution of (growing) protoplanets (Lissauer et al. 2009). The amount of gas that can be bound during the protoplanetary disc phase affects the long-term evolution of super-Earths and mini-Neptunes (Ikoma & Genda 2006; Ikoma & Hori 2012; Lopez et al. 2012).

The gravitationally perturbed flow pattern also affects the behavior of particles. Weidenschilling & Davis (1985) and Paardekooper (2007) investigated the accretion potential of (small) particles. The secular particle-planet interaction has been studied more generally by Muto & Inutsuka (2009). Of special importance in the context of this work is the new 'pebble-accretion' mechanism, where protoplanets quickly accrete small particles, as found by both numerical simulations (Lambrechts & Johansen 2012; Morbidelli & Nesvorny 2012) as well as analytical estimates (Ormel & Klahr 2010; Perets & Murray-Clay 2011). The latter studies however did not account for the modification of the gas flow by the gravity of the protoplanet – the topic of this paper.

The goal of this paper is to obtain a quantitative description of the density structure and the flow (gas velocity) in the vicinity of a gravitating body – in particularly, a pro-

toplanet in a Keplerian-rotating disc – and to assess the role of key parameters like: the headwind, shear, and planet mass. The low-mass planet regime under consideration is characterized by the following scale hierarchy:

$$R < R_b < R_h < H, \qquad (3)$$

where H is the scaleheight of the disc, R the radius of perturber, and R_h the Hill radius

$$R_h \equiv a_0 \left(\frac{M_p}{3M_\star}\right)^{1/3} \qquad (4)$$

(with $M_\star$ the stellar mass) – the scale on which the solar gravity rivals that of the perturber. At the lower range, $R \simeq R_b$, bodies are about $\sim 10^3$ km in size, or 10^{-3}–10^{-2} $M_\oplus$ in mass. With increasing mass both R_b and R_h increase, but the ratio R_h/R_b decreases. At the high-mass end of inequality (3) $R_b \simeq R_h \simeq H$. This corresponds to masses of ~ 10 $M_\oplus$, somewhat larger for the outer disc.

One key approximation that is employed is to neglect contributions originating from the Lindblad region, i.e., the distance $x \sim H$, where shock waves are excited. Resolving the shock at these distances is important for calculating the torque that is exerted on the planets, which determines the orbital evolution (migration) of the planet. However, as an approximation for the flow close to the planets, i.e., on scales $\ll H$, Paardekooper & Papaloizou (2009) argued that it is justifiable to omit the contributions arising from the Lindblad torque region. That is, they showed that this procedure, referred to as 'torque cut-off', is permissible – up to levels of $\sim 10\%$ accuracy – provided that the softening radius, which is customary applied to smoothen the gravitational potential in numerical simulations, is chosen small enough. In this study no softening is present; instead the numerical setup is characterized by a *surface* (inner boundary condition). Avoiding the softening is advantageous, since it is a parameter that, unless carefully chosen, could affect the outcome of the numerical experiment (Dong et al. 2011; Müller et al. 2012).

These considerations imply that the flow past the protoplanet is subsonic. A further assumption is that the flow is two dimensional (2D), which allows us to formulate the flow in terms of a single scalar quantity, the stream function Ψ. Employing the 2D assumption significantly reduces the complexity of the problem (e.g., Korycansky & Papaloizou 1996). Extending the stream function formulation to 3D configurations is straightforward for axisymmetric flows (Lee & Stahler 2011), but much more difficult – often unpractical – for truly 3D flows. Similar simplifying assumptions are that the flow is inviscid and steady (non-turbulent). These idealizations allow us to conduct a thorough parameter study for the flow pattern in the vicinity of the perturbing body, making a systematic investigating of the sensitivity of the flow pattern to the various parameters involved (protoplanet mass, nebular headwind, equation of state, numerical parameters) possible.

The structure of the paper is as follows. In Section 2 we formulate the problem and the underlying (inviscid) fluid equations. In Section 3 a first analytic model for the flow pattern is presented by a linear perturbation analysis. Section 4 highlights the key results obtained from a numerical parameter study. Section 5 a more complete analytic model is given, which describes the critical atmosphere region, un-

der the approximation that the density is a radial function. In Section 6 the analytic model for the gas flow is used to numerically integrate trajectories of small particles in order to assess their accretion behavior. Further implications are discussed in Section 7. Section 8 presents the conclusions.

2 STREAM FUNCTION FORMULATION

In this section the equations of continuity and force-balance (Euler) are rewritten in terms of Bernoulli's equation and a diffusion equation for the stream function Ψ – the quantity that together with the surface density Σ characterizes the flow. The numerical solution to these equations is presented in Section 4 and an analytical approximation is given in Section 5. A key feature of the approach is to connect the local solution near the perturber to the unperturbed solutions at large radii – the far field. The far field flow pattern is assumed to be known and specified by the following constant quantities: surface density (Σ_∞), sound speed (c_∞), vorticity (ω_∞), and headwind (v_{hw}).

2.1 The stream function and far field solution

The 2D shearing-sheet approximation is adopted, with the centre of the coordinate frame rotating at an angular frequency equal to the local orbital frequency Ω_0. In the absence of a perturbing body the flow is, without loss of generality, assumed to be directed in the negative y-direction:

$$\boldsymbol{v}_\infty = (-v_{\text{hw}} - q\Omega_0 x)\boldsymbol{e}_y = (-v_{\text{hw}} + w_\infty x)\boldsymbol{e}_y, \quad (5)$$

where q is the dependence of Ω on disc radius, $\Omega \propto a^{-q}$ at $a = a_0$. All subscripts involving '∞' refer to the far field (unperturbed) solution. Instead of q the linear shear can be quantified by the vorticity in the far field:

$$\boldsymbol{\omega}_\infty = \omega_\infty \boldsymbol{e}_z = \nabla \times \boldsymbol{v}_\infty = -q\Omega_0 \boldsymbol{e}_z. \quad (6)$$

In a Keplerian disc, $q = 3/2$ and $w_\infty = -3\Omega_0/2$.

The 2D stream function, $\boldsymbol{\Psi} = \Psi\boldsymbol{e}_z$, is defined such that it satisfies the continuity equation in steady state, $\nabla \cdot \Sigma\boldsymbol{v} = 0$:

$$\Sigma\boldsymbol{v} \equiv \nabla \times \Psi\boldsymbol{e}_z. \quad (7)$$

In the far field, $\Sigma = \Sigma_\infty$ is constant and Ψ becomes

$$\Psi_\infty = \left(v_{\text{hw}}x - \frac{1}{2}\omega_\infty x^2\right)\Sigma_\infty. \quad (8)$$

Dividing the continuity equation (7) by Σ and taking the curl we obtain the vorticity of the flow:

$$\omega = \boldsymbol{e}_z \cdot \nabla \times \boldsymbol{v} = \boldsymbol{e}_z \cdot \left(\nabla \times \frac{\nabla \times \Psi}{\Sigma}\right) = -\nabla \cdot (\frac{1}{\Sigma}\nabla\Psi), \quad (9)$$

where we used the (general) vector identity $\boldsymbol{e}_z \cdot \nabla \times \boldsymbol{A} = -\nabla \cdot (\boldsymbol{e}_z \times \boldsymbol{A})$ and the 2D-specific

$$\nabla\Psi = \boldsymbol{e}_z \times (\nabla \times \Psi\boldsymbol{e}_z). \quad (10)$$

Furthermore, the vortensity $(2\Omega_0 + \omega)/\Sigma$, is conserved along streamlines.[2] Since Σ and ω are constant in the far field, the

vortensity is constant everywhere and ω can be expressed in terms of Σ:

$$\omega = (2\Omega_0 + \omega_\infty)\frac{\Sigma}{\Sigma_\infty} - 2\Omega_0; \quad (11)$$

and inserted in equation (9) to obtain

$$\nabla \cdot \frac{1}{\Sigma}\nabla\Psi = -\tilde{\omega}\frac{\Sigma}{\Sigma_\infty} + 2\Omega_0, \quad (12)$$

where $\tilde{\omega} = 2\Omega_0 + \omega_\infty$ ($= +\Omega_0/2$ in a Keplerian disc). Thus, Ψ obeys a diffusion equation in which both the diffusion coefficient ($1/\Sigma$) and the source term (the RHS of equation 12) are functions of Σ. If the background flow is shear-free (headwind only) the source term is zero. If in addition the flow is incompressible Laplace equation is obtained: $\nabla^2\Psi = 0$. For the general case, however, both Ψ and Σ are unknown.

2.2 Bernoulli's equation

To solve the degeneracy between Σ and Ψ, equation (12) is supplemented by the Euler equation (force balance). In the uniformly *rotating* reference system that is considered here, the Euler equation contains fiducial forces:

$$\frac{\partial\boldsymbol{v}}{\partial t} + \boldsymbol{v}\cdot\nabla\boldsymbol{v} = -2\boldsymbol{\Omega}_0 \times \boldsymbol{v} - \boldsymbol{\Omega}_0 \times (\boldsymbol{\Omega}_0 \times \boldsymbol{r}) - \frac{1}{\Sigma}\nabla P - \nabla\Phi_g, \quad (13)$$

where Φ_g is the combined gravitational potential (of the planet and the star) acting on the fluid element. The pressure gradient term $\nabla P/\Sigma$ is split into a global contribution, which gives rise to the headwind, and a local perturbation caused by the planet. The global term equals $(dP_\infty/dr)/\Sigma_\infty \equiv -2\eta v_k\Omega_0 = -2v_{\text{hw}}\Omega_0$ (see equation 2) and is added to equation (13) such that $\nabla P/\Sigma$ denotes the perturbation. In addition, it can be shown that the centrifugal force term $(-\boldsymbol{\Omega}_0 \times (\boldsymbol{\Omega}_0 \times \boldsymbol{r}) = -\Omega_0 r^2)$ and the solar force term $(\nabla\Phi_{\text{sun}})$ combine into $2q\boldsymbol{\Omega_0} \times \boldsymbol{e}_x$. Since by assumption the flow is steady ($\partial/\partial t = 0$), equation (13) reads

$$\boldsymbol{v} \cdot \nabla\boldsymbol{v} = -2\boldsymbol{\Omega}_0 \times \boldsymbol{v} - \frac{1}{\Sigma}\nabla P + (2q\Omega_0^2 x + 2v_{\text{hw}}\Omega_0)\boldsymbol{e}_x - \nabla\Phi_P, \quad (14)$$

where Φ_P is solely due to the gravitating body at the centre of the reference frame and ∇P corresponds to the pressure perturbations induced by it. In the far field the LHS as well as the pressure and potential terms on the RHS of equation (14) vanish; and it can be verified that equation (5) is a solution to equation (14).

Using the identity $\frac{1}{2}\nabla v^2 = \boldsymbol{v} \cdot \nabla\boldsymbol{v} + \boldsymbol{v} \times \nabla \times \boldsymbol{v}$ equation (14) transforms into:

$$2\boldsymbol{\Omega_0} \times \boldsymbol{v} - \boldsymbol{v} \times \nabla \times \boldsymbol{v} = -\frac{1}{2}\nabla v^2 - \frac{1}{\Sigma}\nabla P \quad (15)$$
$$- \nabla\left(\Phi_P - q\Omega_0 x^2 - 2v_{\text{hw}}\Omega_0 x\right),$$

or, in terms of the vorticity $\boldsymbol{\omega} = \nabla \times \boldsymbol{v}$:

$$\boldsymbol{v} \times (\boldsymbol{\omega} + 2\Omega_0\boldsymbol{e}_z) \equiv \nabla B \quad (16)$$

with B the Bernoulli function

$$B = \frac{1}{2}v^2 + W + \Phi_P + w_\infty\Omega_0 x^2 - 2v_{\text{hw}}\Omega_0 x. \quad (17)$$

In equation (16) it was further assumed that the flow is barotropic:

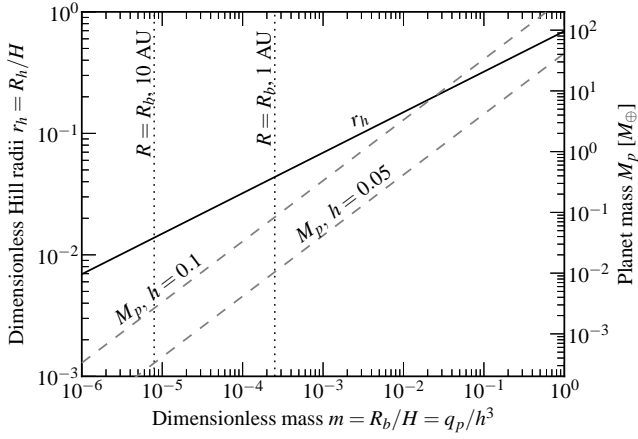$$\frac{\nabla P}{\Sigma} = \nabla \int \frac{dP}{\Sigma} \equiv \nabla W \quad (18)$$

---

[2] See e.g., Landau & Lifshitz (1959) for a proof. Morover, conservation of vortensity implies that the flow is barotropic (equation 18).

Figure 1. Left y-axis: the dimensionless Hill radius r_h as function of mass parameter $m \equiv R_b/H$ (solid line). Right y-axis: the perturber mass M_p corresponding to m for two values of the disk aspect ratio $h = H/a_0$ (dashed lines). For the conversion of q_p to M_p the star was assumed to be of solar mass. Vertical dotted lines show the mass where $R = R_b$, the point where the embryo starts to bind the nebular gas, at distances of 1 AU and 10 AU.

Figure 2. (gray curves) The enthalpy function W (equation 28) as function of density for several values of the transition density: $\Sigma_T = 10, 10^3$ and ∞ (isothermal). (black curve) the LHS of equation (26) for a value for $\frac{1}{2}|\nabla\Psi|^2 = 10^4$. The minimum density $f_{\min}$ for which the Bernoulli equation will obtain real solutions is indicated by an open circle.

with W the enthalpy. In the far field W is assumed to be zero, $W(\Sigma_\infty) = 0$, and the Bernouilli function reduces to

$$B_\infty = \frac{1}{2}v_\infty^2 + w_\infty\Omega_0 x^2 - 2v_{\mathrm{hw}}\Omega_0 x \qquad (19)$$
$$= \frac{1}{2}v_{\mathrm{hw}}^2 - v_{\mathrm{hw}}(2\Omega_0 + \omega_\infty)x + \frac{1}{2}\omega_\infty(2\Omega_0 + \omega_\infty)x^2$$

where equation (5) has been inserted for v_∞.

Since the LHS of equation (16) is orthogonal to $\boldsymbol{v}$, it vanishes upon integration along a streamline. This implies that B is conserved along streamlines (Bernoulli equation). To find the relation between B and Ψ, equation (7) is inserted into equation (16). The LHS of equation (16) is then written in terms of Ψ:

$$\frac{\nabla \times \Psi \boldsymbol{e}_z}{\Sigma} \times \frac{\Sigma}{\Sigma_\infty}\tilde{w}\boldsymbol{e}_z = -\frac{\tilde{w}}{\Sigma_\infty}\nabla\Psi = \nabla B, \qquad (20)$$

where equation (11) and identity (10) are used. As $\tilde{\omega}$ and Σ_∞ are constant, equation (20) simply implies that B is a linear function of Ψ:

$$B(\Psi) = -\frac{\tilde{w}}{\Sigma_\infty}\Psi + \frac{1}{2}v_{\mathrm{hw}}^2, \qquad (21)$$

where the integration constant has been defined such that $B(\Psi_\infty) = B_\infty$ (equation 19).

Together, equations (17), (21) provide a second relation between Ψ and Σ:

$$\frac{1}{2}\frac{|\nabla\Psi|^2}{\Sigma^2} - \frac{v_{\mathrm{hw}}^2}{2} + \frac{\tilde{\omega}}{\Sigma_\infty}\Psi + W + \Phi_P + w_\infty\Omega_0 x^2 - 2v_{\mathrm{hw}}\Omega_0 x = 0. \qquad (22)$$

2.3   Units and nondimensionalisation

For our problem it is natural to measure frequencies ($\omega, \tilde{\omega}$ and Ω_0) in terms of Ω_0 and densities in terms of Σ_∞. A natural length unit is not as obvious, since both the Bondi radius, the Hill radius, and the scaleheight of the disk H could qualify. Here we adopt the scaleheight as the length
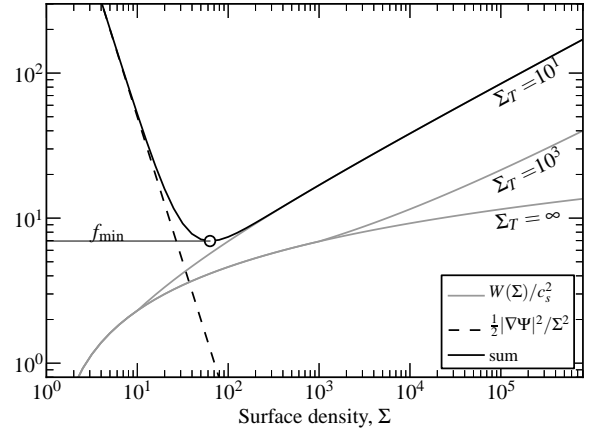
unit, which implies that the unit of velocity is c_∞. The dimensionless disk headwind $\mathcal{M}_{\mathrm{hw}} = v_{\mathrm{hw}}/c_s$ is referred to as the Mach number of the headwind. Because R_b scales with the perturber mass, the dimensionless Bondi unit is also a dimensionless mass:

$$m \equiv \frac{R_b}{H} = \frac{GM_p}{H^3\Omega_0^2} = \frac{q_p}{h^3} \qquad (23)$$

where $q_p = M_p/M_\star$ and $h = H/a_0$ the aspect ratio of the disk. We will use m as the parameter for the mass of the perturbing body. The dimensionless Hill radius can be written

$$r_h = \frac{R_h}{H} = \left(\frac{q_p}{3h^3}\right)^{1/3} = (m/3)^{1/3}. \qquad (24)$$

Figure 1 shows the relation among these quantities as function of the mass parameter m. The regime $m \ll 1$ applies in this paper (low mass limit). Small bodies start to bind an atmosphere when their physical radius starts to exceed the Bondi radius, $R \simeq R_b$. This correspond to an m-value of $m \sim \sqrt{M_\star/\rho_s a_0^3}$ where ρ_s is the internal density of the body. With increasing mass the Bondi and Hill radius start to converge on each other. The point $m \sim 1$ signifies the transition to the high mass regime (for which $R_b > R_h > H$) which is not considered here.

In nondimensional units the diffusion equation (12) and Bernoulli equation (22) read:

$$\nabla \cdot \frac{1}{\Sigma}\nabla\Psi = -\tilde{\omega}\Sigma + 2 \qquad (25)$$

$$\frac{1}{2}\frac{|\nabla\Psi|^2}{\Sigma^2} + W(\Sigma) = -\tilde{\omega}\Psi + \frac{m}{r} + \frac{\mathcal{M}_{\mathrm{hw}}^2}{2} - w_\infty x^2 + 2\mathcal{M}_{\mathrm{hw}}x. \qquad (26)$$

These are two equations for the two unknown quantities, Σ and Ψ. The unperturbed solution ($\Sigma = \Sigma_\infty = 1$; $\Psi = \Psi_\infty$) is obtained when $m = 0$, as it was specified that $W(\Sigma = 1) = 0$.
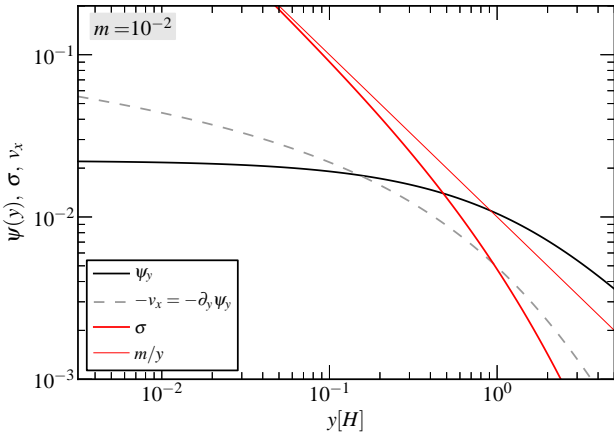
Figure 3. The perturbed stream function ψ_y (black solid curve) and the radial velocity $-v_x$ as function of y in the linear approximation of the linear model for a mass parameter of $m = 10^{-2}$. The perturbed surface density which follows from equation (31) is given by the red thick line. The red thin line gives σ in the hydrostatic limit: $\sigma = m/r$.

2.4 Equation of state (EOS)

These equations are supplemented by an equation of state (EOS). We adopt:

$$P = \begin{cases} c_\infty^2 \Sigma & (\Sigma \leqslant \Sigma_T) \\ c_\infty^2 \Sigma_T \left(\dfrac{\Sigma}{\Sigma_T}\right)^\gamma & (\Sigma > \Sigma_T); \end{cases} \qquad (27)$$

that is, the EOS changes from isothermal to adiabatic at a transition density Σ_T. This prescription approximates the structure of embedded protoplanets in disks (see Inaba & Ikoma 2003; Ormel & Kobayashi 2012). Thus, Σ_T is a proxy of the thermodynamic state of the atmosphere, signifying the point where cooling becomes ineffective. Larger (grain) opacities and more luminous protoplanets will have a smaller isothermal layer, meaning a lower Σ_T.

The enthalpy, through the definition in equation (18), becomes (in units where $c_\infty = 1$):

$$W = \begin{cases} \log \Sigma & (\Sigma \leqslant \Sigma_T) \\ \dfrac{\gamma}{\gamma - 1}\left[\left(\dfrac{\Sigma}{\Sigma_T}\right)^{\gamma-1} - 1\right] + \log \Sigma_T & (\Sigma > \Sigma_T) \end{cases} \qquad (28)$$

This equation is plotted as function of Σ in Fig. 2 for several transition densities. In equation (28) the integration constants have been chosen such that W is continuous at Σ_T and $W(0) = 0$. The adiabatic index is fixed at $\gamma = 1.4$.

3 A LINEAR, ANALYTIC SOLUTION TO THE PERTURBED FLOW PATTERN

Assuming that the perturbations are small, equations (25), (26) can be linearized by setting $\Sigma = 1 + \sigma$, $\Psi = \Psi_\infty + \psi$ where σ and ψ are assumed to be small with respect to the unperturbed quantities. Inserting these expressions into equations (25), (26) and keeping only the first order perturbations (that is, ignoring terms of order higher in ψ and σ),

one obtains (see Appendix A for details):

$$\nabla^2 \psi + (\partial_x \sigma)(\mathcal{M}_{\mathrm{hw}} - \omega_\infty x) + \sigma(\omega_\infty + \tilde{\omega}) = 0 \qquad (29)$$

$$\sigma[1 - (\omega_\infty x - \mathcal{M}_{\mathrm{hw}})^2] + (\omega_\infty x - \mathcal{M}_{\mathrm{hw}})(\partial_x \psi) = -\tilde{\omega}\psi + \frac{m}{r} \quad (30)$$

This set of equations, although simpler than the original, still represents a complex partial differential equation (PDE) which generally can be solved only numerically. To nevertheless pursue with an analytical model, two approximations are made:

   (i) The perturbed flow depends only on y, $\psi = \psi(y)$;
   (ii) The limit $x \ll 1$ and $x \ll y$ are considered.

The first approximation implies that the perturbed flow only describes the x component of the velocity. This is reasonable since the y-component of the flow is in any case dominated by the unperturbed solution ($\omega_\infty x \mathbf{e}_y$), whereas v_x is entirely determined by the perturbed component. Thus, $\partial_x \psi = 0$ and $v_x = (\partial_y \psi)/\Sigma \approx \partial_y \psi$ in the perturbed limit. The second assumption implies that the focus lies on the co-orbital region, $x \approx 0$. This is again reasonable as Ψ_∞ is small here. Since terms including x are now small they can be neglected and Equation (30) becomes simply

$$\sigma \approx -\tilde{\omega}\psi + \frac{m}{r}, \qquad (31)$$

where we have also neglected the $\mathcal{M}_{\mathrm{hw}}^2$ term.

With the same argumentation, the middle term in equation (29) can be neglected; inserting equation (31) into equation (29) and substituting y for r (in fact setting $x = 0$) results in an ordinary differential equation (ODE) for $\psi(y)$:

$$\partial_y^2 \psi - 2\tilde{\omega}(1 + \omega_\infty)\psi = -\frac{2(1 + \omega_\infty)}{r}m \qquad (32)$$

The solution to this ODE is denoted ψ_{y0}. Closed-form solution exists, but depend strongly on the value of ω_∞. In a Keplerian disk, $\omega_\infty = -3/2$ it reads:

$$\psi_{y0} = m \frac{[\pi|y| - 2y\,\mathrm{Si}(\tilde{y})]\cos\tilde{y} + 2y\,\mathrm{Ci}(\tilde{y})\sin\tilde{y}}{\sqrt{2}|y|} \qquad (33)$$

where $\tilde{y} = y/\sqrt{2}$ and $\mathrm{Ci}(u)$, $\mathrm{Si}(u)$ the sine and cosine integral functions, defined as

$$\mathrm{Ci}(u) = -\int_u^\infty \frac{\cos(t)}{t}dt; \qquad \mathrm{Si}(u) = \int_0^u \frac{\sin(t)}{t}dt. \qquad (34)$$

The general solution to equation (32) contains two integration constants. These are of sinusoidal nature, $\psi \sim \sin y$, related to the solutions of the homogeneous equation. These oscillatory terms are discarded however, since such oscillatory terms do not decay for $y \to \infty$. Thus, equation (33) only contains the particular solution to equation (32). Note that equation (33) is linear in m.

Equation (33), plotted in Fig. 3, peaks at $y = 0$ for which $\psi_{y0} = \psi_{\mathrm{hs}} \equiv \pi m/\sqrt{2}$. With the caveat that σ is no longer small here and that as a consequence the solution will break down when $y \to 0$, this value of ψ corresponds, in the shear-only case ($\mathcal{M}_{\mathrm{hw}} = 0$), to the widest streamline that undergoes so called horseshoe motion – i.e., where the gas elements upon their approach to the central object make a U-turn. This critical streamline therefore defines the width of the horseshoe region (x_{hs}), which, as already alluded to
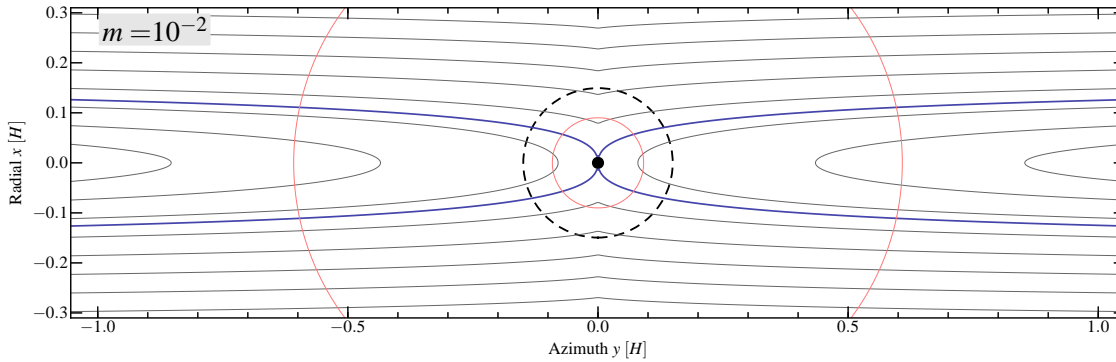
Figure 4. Flow pattern surrounding a protoplanet of dimensionless mass $m = 10^{-2}$ in the linear regime, where perturbations are by construction small. Solid curves are contours of constant $\Psi = \Psi_\infty + \psi_{y0}$, where ψ_{y0} is given by equation 33. The far-field solution (Ψ_∞) does not include a headwind term (shear-only case where $v_{hw} = 0$). Pink circles indicate the perturbation in surface density: contours of $\sigma = 0.01$ and 0.1 are shown. The Hill radius ($r_h = (m/3)^{1/3}$) is given by the dashed circle and the Bondi radius ($r_b = m$) is indicated by the black dot at the centre. These solutions are used as boundary condition for the numerical calculations in Section 4.

in Section 1, is of special significance since it determines the horseshoe torque and connect to the planet's atmosphere. The horseshoe width x_{hs} is obtained by equating ψ_{hs} with the far-field solution, $\Psi_\infty(x_{hs})$, equation (8):

$$x_{hs} = \sqrt{\frac{4\pi}{3\sqrt{2}}m} \approx 1.72\sqrt{m}. \tag{35}$$

($= 1.72 a_0 \sqrt{q_p/h}$ in physical units; see Section 2.3). Equation (35) is in excellent agreement with the findings of Paardekooper & Papaloizou (2009) who found a prefactor of 1.68.

Figure 4 shows the flow pattern in the linearized approximation with $\mathcal{M}_{hw} = 0$ and $m = 10^{-2}$. Solid grey curves are iso-contours of $\Psi_\infty + \psi_{y0}$. The critical horseshoe streamline Ψ_{hs} is highlighted blue. Iso-density lines, which follow from equation (31), are in red. Figure 4 recovers the global features of the perturbed shear flow (the horseshoe orbits in particular) at distances far from the planet (i.e., for $r \gg m$) as seen in many previous works (Masset et al. 2006; Paardekooper & Papaloizou 2009) . For large x the linearized approximation which relies on $x \ll 1$ will break down. For even larger distances, i.e., for $|x| > 2/3$, the PDE describing the system becomes hyperbolic, signifying that a (density) wave is excited. Hyperbolic (wave-like) equations require very different solution techniques (Goldreich & Tremaine 1980; Ward 1986; Tanaka et al. 2002). Including this feature is beyond the scope of this paper.

For the purposes of this paper it is the flow structure in the vicinity of the perturber's Bondi radius that interests us. At these scales, the linear approximation is expected to break down and the nonlinear equations must be solved in earnest. The analytical solution in the linear regime presented by equation (33) will serve as the (outer) boundary conditions for the nonlinear calculation.

4   STEADY-STATE FLOW SIMULATIONS

In this section a strategy to numerically solve the general equations for Σ and Ψ is discussed (Section 4.1). Then, a

parameter study is presented, varying the mass of the perturber and the value of the headwind.

4.1   Numerical algorithm

Equations (25), (26) are solved by iteration, considering one equation at a time. First an initial Ψ is assumed, for example the linear solution, $\Psi_\infty + \psi_{y0}$. Equation (26) is a scalar equation; given $\Psi(\boldsymbol{x})$ and $\nabla\Psi$ it can be inverted to obtain Σ at every grid point. Then, using these values for Σ, equation (25) – a diffusion equation – is solved for Ψ. This completes one cycle.

Thus, when considering equation (26) the RHS is known. The LHS depends on the model for the enthalpy W, for which an equation of state (EOS) needs to be specified. Obtaining Σ from equation (26) is not without ambiguity, as is also illustrated in Fig. 2. Here the LHS of equation (26), $f_{lhs}(\Sigma)$, is plotted as function of Σ for some arbitrarily-chosen value of $|\nabla\Psi|^2$. Starting from $\Sigma = 0$, $f_{lhs}(\Sigma)$ first decreases, reaches a minimum at (Σ_{min}, f_{min}), and then increases towards infinity. Thus, for a given value of the RHS of equation (26) there are either zero, one, or two solutions. In the case of two solutions, we always choose the largest Σ. This is simply because it gives the correct solution in the far field, provided no discontinuities (shocks) are present.

However, during the iteration process, cases are encountered in which the RHS of equation (26) evaluates to less than f_{min}. This is undesired. If this situation occurs, we readjust Ψ by 'mixing' it with the solution obtained in the previous iteration:

$$\Psi = w_n \Psi_N + (1 - w_n)\Psi_P, \tag{36}$$

with Ψ_P the previous solution for the stream function that did satisfy equation (26), Ψ_N the new solution, and w_n a weight. Starting from $w_n = 1$, w_n is adjusted until Ψ satisfies equation (26) again. In runs where w_n in this way is forced to become arbitrary low the iteration procedure clearly has failed. The calculations are then terminated.

The finite volume algorithm FiPy (Guyer et al. 2009),[3]

---

[3] Downloadable at http://www.ctcms.nist.gov/fipy/

Parameter	Symbol	Default	Range	Unit
Resolution	$N_{\rm res}$	200	100—400	
Headwind	$\mathcal{M}_{\rm hw}$		0, 0.05, 0.1	c_s
Mass	m	10^{-2}	10^{-3}—10^{-1}	$h^3 M_\star$
Inner radius	R_1	0.1	10^{-3}—1	R_b
Domain size	$r_{\rm out}$	0.3	0.01—0.6	H
Transition mass	Σ_T	0.1	10—10^3	Σ_∞

Table 1. Default value and range of numerical and physical parameters considered in this study. The last column denotes the unit to convert the dimensionless numbers into physical ones.

is used to solve the partial differential equation (25). A grid and boundary conditions (BCs) need to be specified. It is customary for these kind of simulations to considered a rectangular grid. In this work, however, a polar grid ($r = \sqrt{x^2 + y^2}; \theta = \arctan(y/x)$) is used with the perturbing body located at the centre of the coordinate system. The inner boundary of the grid is located at a radius r_1 from the perturbing body and may correspond to the physical radius of the body.

In FiPy either Ψ or the gradient $\partial_r \Psi$ must be specified as a BC. At the inner boundary ($r = r_1$) the radial velocity, v_r, vanishes. Therefore, $\partial_\theta \Psi = 0$ at the inner surface, and Ψ is constant (say $\Psi = \Psi_1$) on this surface. The value of Ψ_1 is *a priori* unknown, but it can temporarily be set to an arbitrary value since equation (25) will be unaffected by adding a constant to Ψ. Therefore Ψ_1 is fixed at $\Psi_1 = 0$. The outer boundary ($r_{\rm out}$) is then specified by Neumann BCs, i.e., $\partial_r \Psi(r_{\rm out}) = \partial_r(\Psi_\infty + \psi_{y0})$ where the far field solution in polar coordinates reads $\Psi_\infty = -\frac{1}{2}w_n r^2 \cos^2\theta + v_{\rm hw} r \cos\theta$ and ψ_{y0} is given by equation (33).

The obtained solution (with $\Psi_1 = 0$) generally shows a mismatch at the outer boundary, i.e., $\Psi(r_{\rm out}) \neq \Psi_{\rm out}$, where the latter is given by the linear perturbation: $\Psi_{\rm out} = \Psi_\infty(r_{\rm out}) + \psi_{y0}(r_{\rm out})$. Let the difference between Ψ and $\Psi_{\rm out}$ be denoted C_Ψ. Although the constant C_Ψ is irrelevant for the velocity of the flow (which are derivatives of Ψ), it matters for equation (26), since it was assumed in its derivation that Ψ approaches Ψ_∞ in the far field. The constant C_Ψ is obtained by minimizing the relative error at $r = r_{\rm out}$,

$$\sum_i \left(\frac{\Psi_i + C_\Psi - \Psi_{{\rm out},i}}{\Psi_{{\rm out},i}}\right)^2, \qquad (37)$$

with respect to C_Ψ, where the index i refers to the $i^{\rm th}$ azimuthal point on the outer surface. It is then added to the solution obtained by FiPy such that it approximately matches $\Psi_{\rm out}$ at $r_{\rm out}$.

4.2 General results; key parameters

By virtue of the various simplifications that have been employed, the algorithm to solve for the steady-state flow pattern is computationally quite efficient; the CPU time is not much longer than a minute for a typical run on a standard desktop machine at the default resolution of 200 grid points in the radial and azimuthal direction. This allows us to carry out an extensive parameter study, studying the effects of the physical and parameter parameters see Table 1. The key physical parameters of interest here are: the headwind

($v_{\rm hw} = \mathcal{M}_{\rm hw}c_\infty$) and the planet mass (which is expressed in terms of the Hill radius r_h, see Section 2.3).

Not all runs converge. As expected from the discussion in the previous section, runs with a radial width that approaches the scaleheight no longer converge, because the setup does not resolve shocks. Either one of equations (25), (26) then fails to be satisfied. Typically, it is found that models with an outer radius ($r_{\rm out}$) exceeding $\simeq 0.4$ start to slow down significantly (because w_n becomes low) and models with $r_{\rm out} > 0.6$ fail to converge at all. The dependence on the outer radius is therefore investigated, see Section 4.4.

The sensitivity of the flow pattern to the number of grid points in the radial and azimuthal directions (N_r, N_θ) has also been investigated. Generally, we find that convergence is achieved by $N_{\rm res} = 200$, meaning that the $N_{\rm res} = 400$ results did not provide a noticeably different result. But see Section 4.4 for some exceptions.

The flow and density structure interior to the Bondi radius is affected by the inner radius R_1 and transition density Σ_T. These are also varied: R_1 starting from the Bondi radius until $R_h/10^3$ (which corresponds to the true physical radius at 5 AU); and Σ_T is sampled at $10, 10^2$ and 10^3. The density close to $R = R_1$ can become rather large; and due to the conservation of vortensity ($\tilde{\omega}/\Sigma$), if non-zero, a very large azimuthal velocity emerges near the inner radius R_1. The large dynamic range in Σ and $\boldsymbol{v}$ in these cases often proves too much of a burden for the numerical code. However, variations in R_1 and Σ_T are found not to significantly affect the flow pattern outside the Bondi radius.

4.3 Runs without shear or rotation (headwind-only)

In this section all parameters regarding rotation and shear are zero: $\omega_\infty = \tilde{\omega} = \Omega = 0$. Consequently, the outer outer boundary condition $\Psi_{\rm out}$ is set by the far field solution (Ψ_∞) and does not involve ψ_{y0}, as the latter is only applicable for Keplerian shear.

4.3.1 Incompressible runs

When the flow is furthermore incompressible ($\Sigma = \Sigma_\infty = 1$) equation (25) becomes Laplace's equation, $\nabla^2 \Psi = 0$. For a cylindrical geometry, the flow has an analytical solution (e.g., Landau & Lifshitz 1959):

$$\Psi = \mathcal{M}_{\rm hw}\left(r - \frac{r_1^2}{r}\right)\cos\theta = \Psi_\infty - \frac{\mathcal{M}_{\rm hw}r_1^2 \cos\theta}{r}, \qquad (38)$$

where the unperturbed flow is assumed to move in the negative y direction. This solution can be used to test the accuracy of the numerical model.

Figure 5a shows the stream pattern corresponding to the incompressible limit, where Σ is enforced to be unity. In the figure, the direction of the flow is indicated by black arrows, which indicate the direction of the flow and the flow velocity (larger arrows correspond to larger v but there is no absolute scale in any of the figures). Contours of constant Ψ – streamlines – lie parallel to $\boldsymbol{v}$. Note the vertical streamline at $x = 0$ ($\theta = \pi/2$) that must hit the objects due to symmetry considerations. The surface potential ($\Psi_1 = \Psi(r_1)$) is therefore characterized by this value for Ψ; here, $\Psi_1 = 0$.
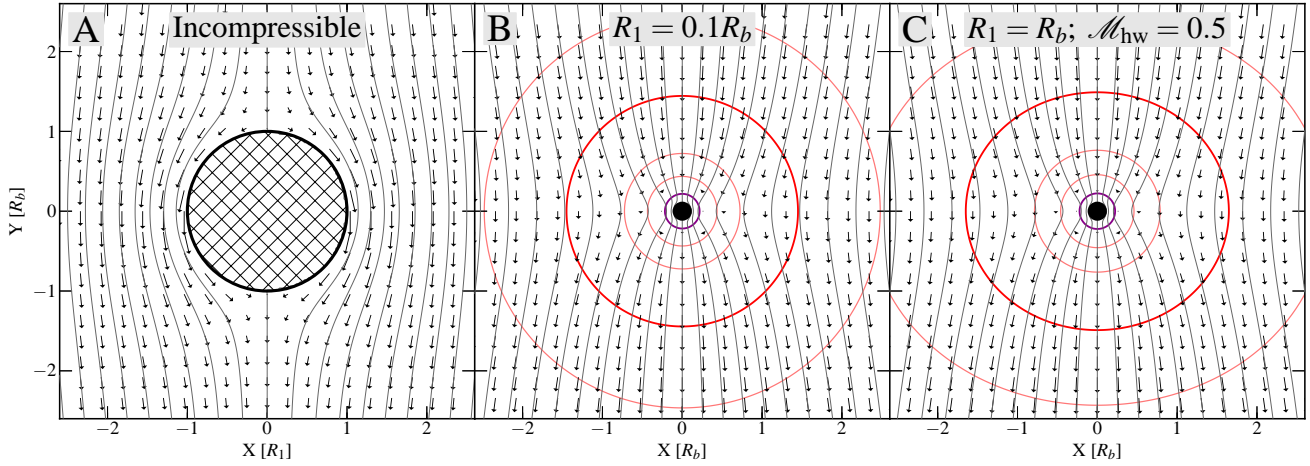
Figure 5. 2D inviscid flow calculations in the case of a pure headwind (no terms involving shear or rotation). (a) Incompressible flow with the Mach number of the headwind equal to 0.1; (b) gravitating flow with the Bondi radius equal to one-tenth of radius of the object; (c) gravitating flow at an increased Mach number of 0.5. In each panel the flow pattern is described by arrows and streamlines (gray curves) that are isocontours of Ψ. There is no absolute scale for the size of the velocity arrows among the panels. Solid, coloured contours indicate gas overdensities (Σ/Σ_∞) of: 1.2, 1.5 (salmon), 2.0 (thick red), 4.0 (salmon), 10, 10^2, 10^3, etc (all magenta). Note the focusing of streamlines starting in (b) and the distortion of the isodensity contours in (c).

The computed flow pattern corresponds very well to the analytical solution (equation 38), but it does not give a perfect match. The small offset in Ψ is caused by the boundary conditions at the (finite) outer radius. Here (at $r = r_{out}$) $\partial_r \Psi = \partial_r \Psi_\infty$, which deviates from equation (38) by a term of $\mathcal{O}(r_{out}^{-2})$. By increasing r_{out} this error can be made arbitrarily small, however.

4.3.2 Compressible, gravitating flow

In Fig. 5b gravity has been including while keeping the flow irrotational. The value of the headwind (v_{hw}) now matters and it is fixed at 10% of the sound speed. The flow pattern is further determined by the ratio of the Bondi radius to the inner radius, $R_1/R_b = 0.1$. Isocontours of Σ are nearly circular and displayed in Fig. 5b,c in red-shaded colours: $\Sigma = 1.2, 1.5, 4$ (salmon), 2 (red), $10, 10^2, 10^3$ (magenta).

For $R_b = R_1$ the flow does not significantly deviate from the incompressible limit. However, when the body increases in mass, it acquires a thick atmosphere. In the hydro*static* limit $\Sigma(r)$ can be obtained by balancing the gravitational force to the pressure support:

$$\frac{1}{\Sigma}\frac{dP}{dr} = -\frac{m}{r^2}, \tag{39}$$

which results in $\Sigma = \Sigma_\infty \exp(m/r)$ for an isothermal EOS. The radius $r = m$ (which is the Bondi radius) signifies the point below which the gas density will increase exponentially. For $r_1 < m$ density gradients becomes very steep, and huge amounts of gas mass can be concentrated towards $r = r_1$ as long as the EOS stays isothermal. Here however the EOS changes at a density $\Sigma_T = 10^2$ (see equation 27), causing a transition to a power-law dependence of Σ with r.

As can been seen in Fig. 5b the (curl-free) flow focuses towards the gravitating body and slows down when it approaches the body. This is simply a consequence of mass conservation: as Σ rises sharply, v has to decrease due to the steady condition that is imposed on the flow. As a result, the

flow converges towards the centre, and then diverges again. The focusing of the gas gives rise to an hourglass pattern for the streamlines.

For a Mach number of 0.1 in Fig. 5b, the density is well-approximated by the hydrostatic limit of solution (39). Never the less the density isocontours are not entirely circular, but the deviation is unnoticeable by eye. For larger values of $\mathcal{M}_{hw}$, however, the isocontours outside the Bondi sphere become more oval-shaped, see Fig. 5c, where the Mach number of the incident flow is increased to 0.5. This trend agrees with the study of Lee & Stahler (2011), who considered an 3D axisymmetric geometry. However, for cases where $\mathcal{M}_{hw} \ll 1$ the density can be well approximated as a function of radius only, $\Sigma = \Sigma(r)$. This finding will be employed in Section 5 to find an analytical model for Ψ.

4.4 Shear-only runs; parameter study

Next, the flow past bodies in a Keplerian potential is considered: i.e., $\omega_\infty = -3/2$ and $\tilde{\omega} = 1/2$ ($\Omega_0 = 1$) and the outer boundary condition at radius r_{out} involves ψ_{y0} (Section 3). The headwind $\mathcal{M}_{hw} = 0$, such that the y-component of the flow velocity always vanishes at $x = 0$. The mass is taken to be $m = 10^{-2}$, which implies a Hill radius of $r_h = 0.15$. In physical units, this mass equals $\sim$0.1–1.0$M_\oplus$ depending on the disc aspect ratio (see Fig. 1). The inner radius is again fixed at $r_1 = 0.1m$ ($R_1 = 0.1R_b$), which implies an inner boundary somewhat larger than the physical radius of the protoplanet. The larger value is adopted for computational reasons; the value of r_1 does not affect the flow pattern *outside* the Bondi radius.

In Fig. 6 the steady flow corresponding to these parameters is presented at three different magnifications. In Fig. 6a the scale of the panel is that of the Hill radius, i.e., the range in both X and Y is $2R_h$. For convenience, following Fig. 5, length units on both axis are given in Bondi radii.
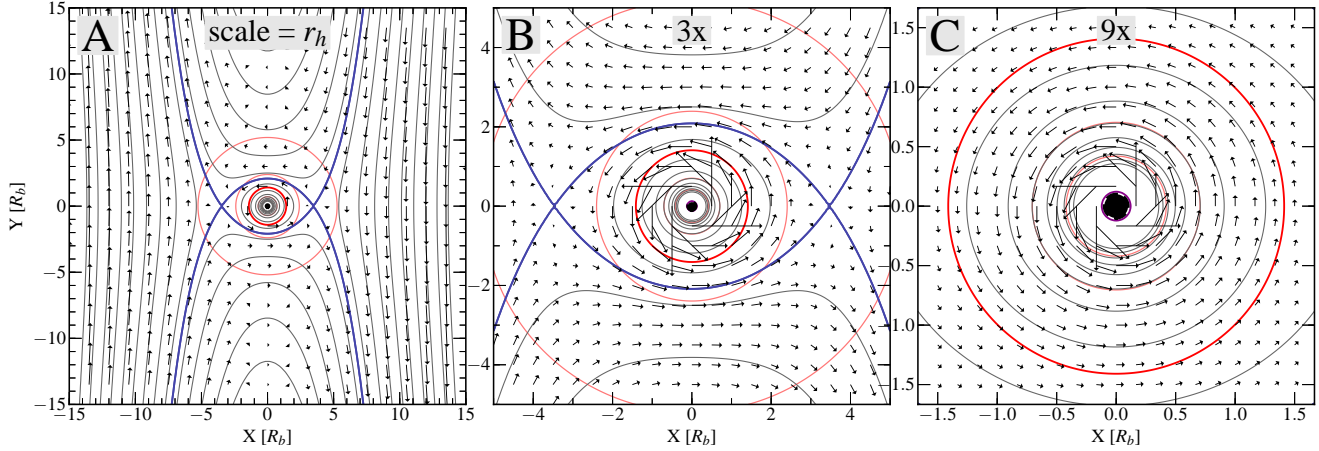
Figure 6. Flow pattern and density contours in a shear-only run (neglecting the headwind contribution) for $m = 10^{-2}$ and an inner radius one-tenth of the Bondi radius. The panels give the flow pattern on scales of: (a) the Hill radius r_h; (b) $r_h/3$; (c) $r_h/9$. See Fig. 5 for a description of the contours. In addition, the solid blue curves correspond to Ψ_X: the isocontour line of Ψ that intersects the stagnation point of the flow on the x-axis (where velocities vanish). This streamline defines the horseshoe region (where streamlines make U-turns) and the atmosphere of the planet (where streamlines are closed).

Figure 6b,c present zoom-ups of the flow in the vicinity of the planet.

The topology of the flow features several qualitatively distinct regions. To the far-left and right, at scales $|x| \gtrsim r_h$, it resembles the unperturbed solution: streamlines are nearly vertical with only little curvature. However, at smaller x-values the planet more strongly affects the flow, giving rise to the horseshoe region, quite similar to the linearized solution of Section 3. The streamline that divides these regions – the separatix streamline Ψ_X – is highlighted. At the point where it crosses the a-axis the flow stagnates: $\boldsymbol{v} = 0$. The x-value of this stagnation point is nonzero, in contrast to the linear solution. A new region, not present in the linear solution, therefore arises: the planet's atmosphere.

Within the atmosphere region streamlines are closed and the gas, which encircles the planet, is bound. The direction of the flow's rotation is prograde (e.g., D'Angelo et al. 2002; Tanigawa et al. 2012). For the shear only runs, it encompasses a region that is quite larger than the Bondi radius, $r = m$. Most of the atmosphere's volume – not necessarily its mass – is therefore of low (nebular) density. At scales $r < r_b$ the density sharply increases. So does the velocity, which becomes more and more azimuthal ($|v_\phi/v_r| \gg 1$). This increase follows from vortensity conservation, i.e., $\omega \simeq \tilde{\omega}\Sigma$. Nevertheless, the atmosphere at this stage is predominantly supported by pressure, instead of rotation.

These results are broadly in agreement with previous studies (e.g., Miki 1982; Korycansky & Papaloizou 1996; Bate et al. 2003; Machida et al. 2010), although usually a more massive planet is considered (with a non-zero softening radius instead of a surface) and the focus lies on resolving the flow pattern on scales $r \gg H$ in order to resolve the spiral wave pattern excited by the Lindblad torques. Nevertheless, the general features described above are all recovered. The steady state solution of Bate et al. (2003) assumes that the planet accretes mass in, essentially, the BHL-regime, which may be appropriate for large planet masses, but requires a
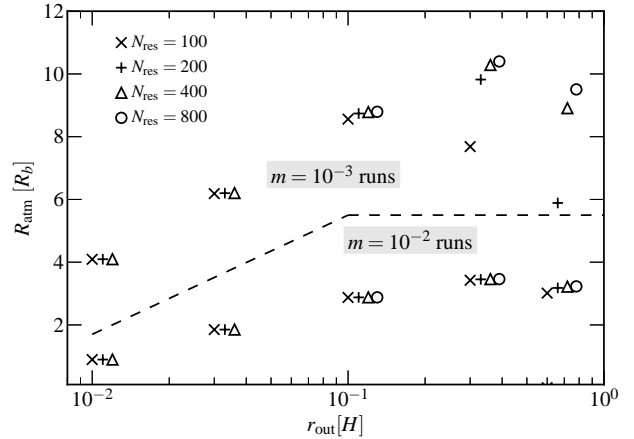

Figure 7. Dependence of the atmosphere size (the stagnation point where the critical streamlines intersect) R_{atm} (given in terms of Bondi radius) on the numerical resolution N_{res} (symbols) and the domain size r_{out} (x-axis). Symbols that corresponds to the same r_{out} are slightly offset for clarity. Results for the $m = 10^{-3}$ runs lie above the dashed auxiliary line; runs with $m = 10^{-2}$ below. This study indicates that convergence is achieved at a large domain size but that especially the low-m runs require a large resolution.

very efficient cooling mechanism in the low planet regime (cf. discussion in Section 1).

The radius of the atmosphere R_{atm} may be defined by the point where the separatix streamlines intersect, i.e., it gives the distance to the stagnation point. Judging from Fig. 6 the atmosphere radius is ≈ 3.5 R_b. In Fig. 7 the dependence of R_{atm} against the two key numerical parameters – the numerical resolution N_{res} and the domain size r_{out} – is investigated both for an $m = 10^{-2}$ and $m = 10^{-3}$ perturber. The numerical resolution varies from $N_{res} = 100$ (these runs take a few seconds to complete on a desktop machine) to $N_{res} = 800$ (runs can approach one hour). The domain size r_{out} goes up to $r_{out} = 0.6$ scaleheights – the maximum where the runs still converge (see Section 4.1). In
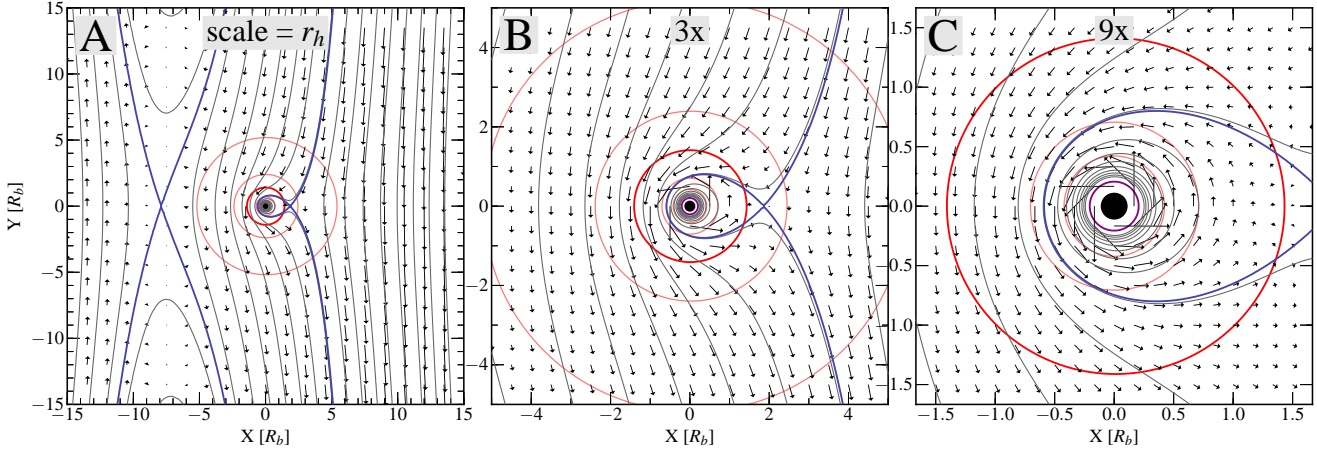
Figure 8. Same as Fig. 6 but also including a headwind of $v_{\rm hw} = 0.1c_\infty$ ($\mathcal{M}_{\rm hw} = 0.1$). There are two solutions for the separatix streamline (in blue): one associated with the horseshoe region, which lies at $x \simeq -10$ in (a); and one circumscribing the planet's atmosphere. Note in (c) that the atmosphere is asymmetrical with nebula material penetrating within a fraction of the Bondi sphere. See the caption of Fig. 5 for the description and labeling of the contour levels.

this figure, the atmosphere radius is also measured in Bondi radii. Note that the $m = 10^{-3}$ runs (which lie above the dashed auxiliary line) have a Bondi radius that is a factor ten smaller than the $m = 10^{-2}$ runs. Thus, in physical units $R_{\rm atm}$ is (as expected) larger for larger m.

Figure 7 shows that in most – but not all – of the runs the numerical resolution hardly affects $R_{\rm atm}$. More significant is the dependence on the domain size $r_{\rm out}$. Figure 7 shows that a larger domain size results in larger atmosphere radii. Clearly, the outer boundary constraints influence the flow pattern to some extent and to be assured of convergence $r_{\rm out}$ must be chosen as large as feasible. However, for the $m = 10^{-3}$ runs the dynamic range, i.e., the ratio of $r_{\rm out}$ to the Bondi radius (m) becomes very large in this way and a high resolution is needed to solve for the flow pattern at every point. But Fig. 7 does show that all models converge for large $r_{\rm out}$ and $N_{\rm res}$. In the following we will therefore stick with the standard of $r_{\rm out} = 0.3$ and $N_{\rm res} = 200$ for the numerical parameters for which we expect the error in $R_{\rm atm}$ to be at most 10%.

4.5 Runs including shear and headwind

Figure 8 shows the steady state flow pattern of a run that includes a nonzero headwind ($\mathcal{M}_{\rm hw} = 0.1$) and a (Keplerian) shear term, again for a mass of $m = 10^{-2}$. The flow topology is quantitatively different from the shear-only case. The combination headwind+shear destroys the symmetry that was previously present along the $x = 0$ axis; the stagnation points are no longer symmetrical around $x = 0$. As a result, there are two separatix streamlines and two solutions for Ψ_X: one that encloses the planet's atmosphere ($\Psi_{\rm atm}$); and one, offset from the planet, that corresponds to the horseshoe region ($\Psi_{\rm hs}$). The planet's atmosphere is sandwiched by flow which moves in the direction of negative y – an effect that is also seen for lower $v_{\rm hw}$. This topology is therefore the rule and the $v_{\rm hw} = 0$ run of Fig. 6 a special symmetric limit.

The position of the separatix streamlines changes according to the planet mass and the value of the headwind.

Figure 9 investigates the effects of varying the headwind ($\mathcal{M}_{\rm hw} = 0$, 0.05 and 0.1; from top to bottom) and the planet mass ($m = 3 \times 10^{-3}$, 10^{-2} and 3×10^{-2}; from left to right). Thus, Fig. 9a corresponds to Fig. 6 and Fig. 9d to Fig. 8. The scale of each panel is again the Hill radius. Note that the left-most highlighted streamline in the runs with a modest headwind ($\mathcal{M}_{\rm hw} = 0.05$; panels d–f) is not associated with any stagnation point. Instead, it just happens to have the same value as that of the atmosphere streamline $\Psi_{\rm atm}$ that encloses the atmosphere of the planet.

Despite its importance, many works studying the flow behavior tend to neglect the headwind term (but see, e.g., Paardekooper 2009 for the implications of a large headwind on planet migration). In particular, the headwind may affect the accretion efficiency of small particles. Comparing the $\mathcal{M}_{\rm hw} \neq 0$ to the $\mathcal{M}_{\rm hw} = 0$ runs, it is noted that in the former the atmosphere region is much reduced. Small particles can be brought closer to the planet, even within a fraction of the Bondi radius. From this observation it seems that a (modest) headwind may actually promote protoplanet growth. Section 6 assesses this issue in more detail.

The asymmetry of the atmosphere is quantified in Fig. 10, which plots the radius of the atmosphere as function of the mass of the planet for runs with and without a headwind. The size of the atmosphere $R_{\rm atm}^+$ ($R_{\rm atm}^-$) is defined to be the absolute value of the x-coordinate where $\Psi_{\rm atm}$ intersects the positive (negative) x-axis. For $\mathcal{M}_{\rm hw} = 0$, $R_{\rm atm}^+ = R_{\rm atm}^-$ is seen to follow a trend that lies between the Bondi radius and the Hill radius. Thus, for a small planet it is significantly larger than the Bondi radius (cf. Fig. 6). For $\mathcal{M}_{\rm hw} \neq 0$ the symmetry breaking causes two solutions with $R_{\rm atm}^+ > R_{\rm atm}^-$. The negative solution always lies within the Bondi radius. In addition, $R_{\rm atm}^-$ and $R_{\rm atm}^+$ decrease with increasing headwind.

5 ANALYTICAL DESCRIPTION OF THE FLOW PATTERN NEAR THE PERTURBER

From the numerical results, it was found that the density Σ is primarily a function of r. This can be understood
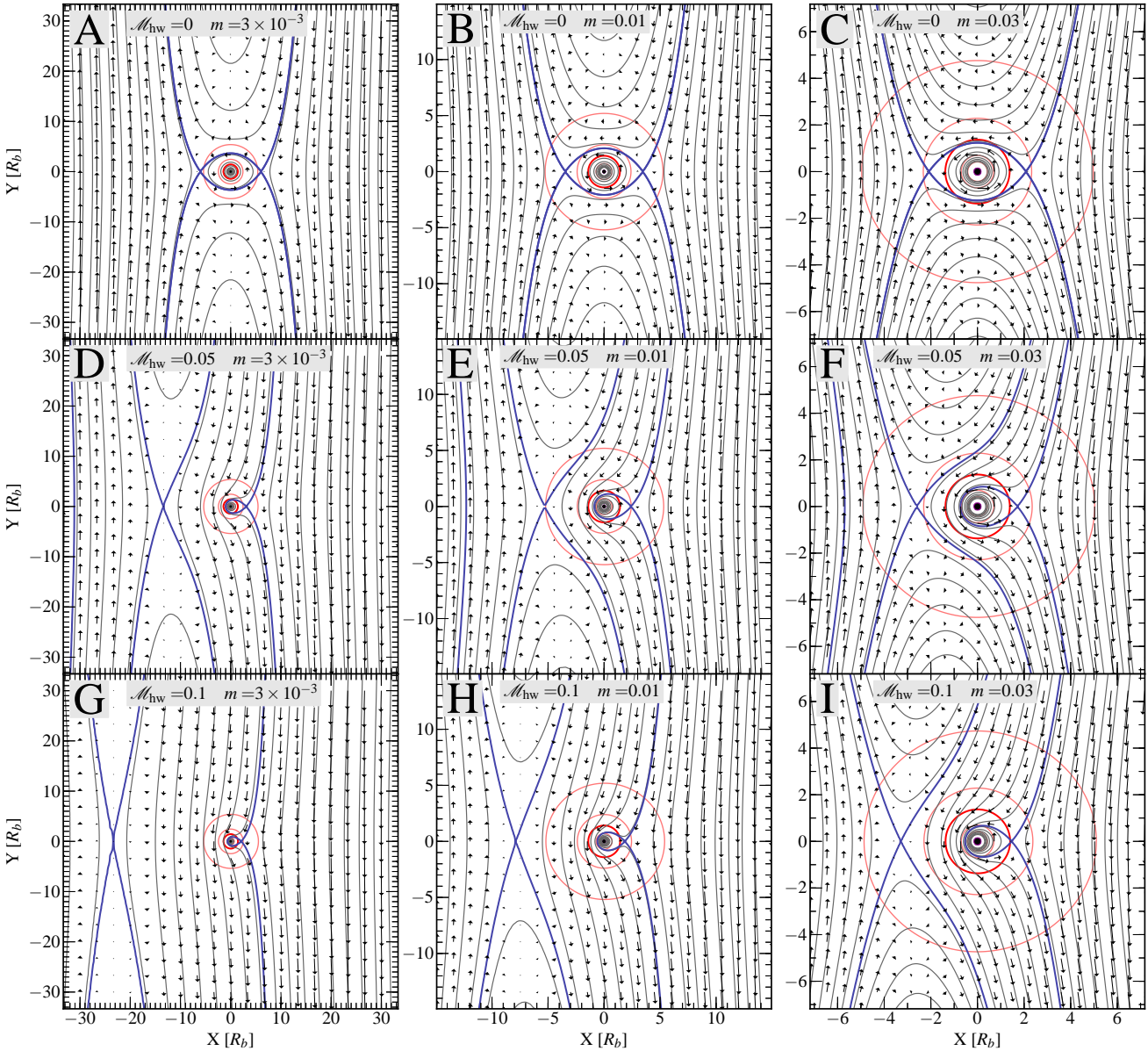
Figure 9. Trends with increasing planet mass (from left to right) and increasing headwind (from top to bottom). Each panel covers a region two Hill radii in width, centred on the planet.

from comparing the terms appearing in equation (26). When $r \lesssim m$ the term representing the planet's potential, m/r, is dominant, whereas for large radius the first order solution of equation (26) is, by definition, Ψ_∞. At $r \sim m$, then, the Bernoulli equation approximately reduces to $W(\Sigma) = m/r$, which in the isothermal regime leads to $\Sigma = \exp(m/r)$.

The solution $\Sigma = \exp(m/r)$ corresponds to an isothermal atmosphere in hydrostatic equilibrium. In the following, the hydrostatic solution is supposed to hold for the density structure, but not for the flow itself which is steady, but not static. The diffusion equation (25) is then left to solve. It can be written as

$$-\nabla \log \Sigma \cdot \nabla \Psi + \nabla^2 \Psi = -\Sigma(\tilde{\omega}\Sigma - 2) \qquad (40)$$

or in terms of the derivatives towards r and θ:

$$r^2 \partial_{rr}\Psi + \left(r - r^2 \frac{d \log \Sigma}{dr}\right)\partial_r \Psi + \partial_{\theta\theta}\Psi = -\Sigma r^2(\tilde{\omega}\Sigma - 2), \quad (41)$$

when the density is a function of radius only. The term in brackets on the LHS becomes $(r+m)\partial_r\Psi$ for $\Sigma = \exp(m/r)$.

This partial differential equation (PDE) can be solved by adopting the *Ansatz* that Ψ is a superposition of a homogeneous solution, $\Psi_{\mathrm{hom}}(r, \theta)$, and a particular solution $\Psi_r(r)$:

$$\Psi(r, \theta) \equiv \Psi_{\mathrm{hom}}(r, \theta) + \Psi_r(r); \qquad (42)$$

i.e., where Ψ_{hom} satisfies the homogeneous PDE

$$r^2 \partial_{rr}\Psi_{\mathrm{hom}} + (m+r)\partial_r\Psi_{\mathrm{hom}} + \partial_{\theta\theta}\Psi_{\mathrm{hom}} = 0, \qquad (43)$$
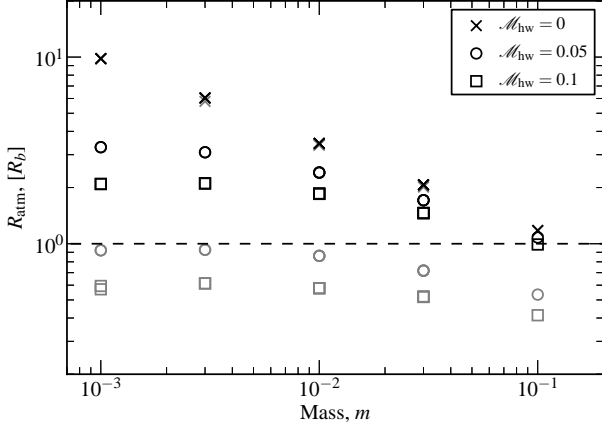
Figure 10. Atmosphere size as defined by the distance to the stagnation points. The solution corresponding to the positive x-axis (R_{atm}^+) is plotted by black symbols, while gray symbols correspond to R_{atm}^-. In the shear-only case ($\mathcal{M}_{\text{hw}} = 0$) symmetry ensures that $R_{\text{atm}}^+ = R_{\text{atm}}^+$. A headwind breaks the symmetry and results in a noticeable decrease, of especially R_{atm}^-.

and $\Psi_r(r)$ the ordinary differential equation (ODE)

$$r^2 \Psi_r'' + (m+r)\Psi_r' = e^{m/r} r^2 \left[2 - \tilde{\omega} e^{m/r} \right], \tag{44}$$

where primes denote derivatives to r.

This simplifies the problem greatly. Equation (43) resembles Laplace equation but contains an additional $\partial_r \Psi$ term. Equation (44) only contains r as the variable. Closed form solutions are possible.

5.1 Solving equation (43)

The strategy to solve this PDE is the same as with Laplace's equation. Assuming that the solution is separable, $\Psi_{\text{hom}}(r, \theta) = f(r)g(\theta)$, equation (43) reduces to two ODEs:

$$r^2 f'' + (m+r)f' - n^2 f = 0 \tag{45}$$

for the radial part; and

$$\frac{d^2 g}{d\theta^2} + n^2 g = 0 \tag{46}$$

for the angular part. Thus, $g(\theta) = \cos n\theta$, where the sine solutions are discarded because of symmetry considerations – the far field solution Ψ_∞ only contains cosine terms. Clearly, $n = \pm 1$ correspond to the case of uniform flow (headwind) and $n = \pm 2$ holds for the shear case. For $|n| \leqslant 2$ the solutions to equation (45), denoted $f_n(r)$, read:

$$f_n(r) = \begin{cases} 12 \left[e^{m/r} \left(\dfrac{2r}{m} - \dfrac{6r^2}{m^2} \right) + 1 + \dfrac{4r}{m} + \dfrac{6r^2}{m^2} \right] & (n = -2) \\[2ex] \dfrac{2r}{m} e^{m/r} - \dfrac{r}{m} - 1 & (n = -1) \\[2ex] 1 & (n = 0) \\[2ex] 1 + \dfrac{r}{m} & (n = 1) \\[2ex] \dfrac{1}{6} + \dfrac{2r}{3m} + \dfrac{r^2}{m^2} & (n = 2) \end{cases} \tag{47}$$

For $r \gg m$, $f_n(r)$ is of $\mathcal{O}([r/m]^n)$, also for negative n. The general solution for Ψ_{hom} therefore reads

$$\Psi_{\text{hom}}(r, \theta) = \sum_{n=-2}^{2} c_n f_n(r) \cos n\theta, \tag{48}$$

with c_n a constant that must be obtained from the boundary conditions.

5.2 Solving equation (44)

Equation (44) is only of first order in the derivative of Ψ_r, Ψ_r', and exhibits an analytical solution. For $\Psi'(r)$ it reads

$$\Psi_r'(r) = \frac{e^{\frac{m}{r}} \left[m^2 \tilde{\omega} \text{Ei}\left(\frac{m}{r}\right) - \tilde{\omega} r(m+r)e^{\frac{m}{r}} + 2(r^2 + C_1) \right]}{2r}, \tag{49}$$

where $\text{Ei}(x)$ is the exponential integral (see equation B2) and C_1 a constant of integration. This constant determines the direction of rotation (prograde or retrograde) of the gas flow within the atmosphere. Equation (49) can be integrated once more to provide Ψ_r (see Appendix B), which introduces another constant of integration, C_2.

5.3 Setting the integration constants

We first consider the limit $r \gg m$, where the solution $\Psi_{\text{hom}} + \Psi_r$ should converge to the far-field solution, Ψ_∞. In the limit $r \gg m$, equation (49) can be approximated as

$$\Psi_r'(r) \approx \left(1 - \frac{\tilde{\omega}}{2} \right) r + \left(1 - \frac{3}{2}\tilde{\omega} \right) m, \tag{50}$$

independent of C_1. Integrating once more:

$$\Psi(r) \approx -\frac{1}{4}\omega_\infty r^2 + \left(1 - \frac{3\tilde{\omega}}{2} \right) mr + \dots \tag{51}$$

where ω_∞ has been used instead of $\tilde{\omega}$ in the first term. Only terms of $\mathcal{O}(r^1)$ or higher are included in the expansion. For $r \gg m$, the linear term is small and will be neglected. Similarly, the expansion of Ψ_{hom} gives

$$\Psi_{\text{hom}} \approx c_2 \frac{r^2}{m^2} \cos 2\theta - c_1 \frac{r}{m} \cos \theta \tag{52}$$

It is now required that the solution $\Psi_{\text{hom}} + \Psi_r$ matches the far-field solution Ψ_∞ (equation 8), which can be written as

$$\Psi_\infty = -\frac{\omega_\infty r^2}{4} \cos 2\theta + v_{\text{hw}} r \cos \theta - \frac{\omega_\infty r^2}{4}. \tag{53}$$

The three terms correspond respectively to the $n = 2$ (shear) term of the homogeneous solution, the $n = 1$ (headwind) term, and the leading term of equation (51). Thus the integration constants of the homogeneous solution, c_1 and c_2, simply follow from the requirement that the leading terms should match Ψ_∞ in the far field:

$$c_2 = -\frac{\omega_\infty m^2}{4}; \tag{54}$$

$$c_1 = mv_{\text{hw}}. \tag{55}$$

The c_{-1} and c_{-2} constants can be found by demanding
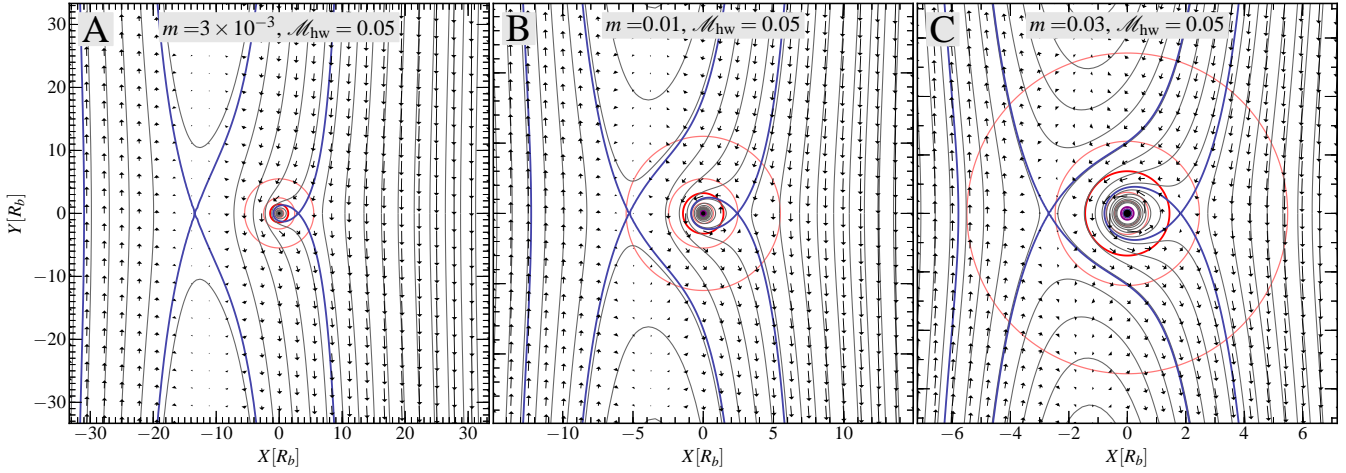
Figure 11. Flow patterns drawn from the analytical prescription for Ψ outlined in Section 5 for perturber masses of: (a) $m = 3 \times 10^{-3}$, (b) $m = 10^{-2}$, and (c) $m = 3 \times 10^{-2}$. The headwind is $\mathcal{M} = 0.05$ in each panel and the control parameter y_c is set at 0.05 as argued in the text. These panels should be compared to the middle row of Fig. 9.

that Ψ at the inner boundary ($r = r_1$) is a constant, i.e., no azimuthal dependence. This gives

$$c_{-2} = -c_2 \frac{f_2(r_1)}{f_{-2}(r_1)}; \tag{56}$$

$$c_{-1} = -c_1 \frac{f_1(r_1)}{f_{-1}(r_1)}. \tag{57}$$

But these terms do not affect the solution for $r \simeq m$ and are rather unimportant. One may neglect these and the negative n terms of equation (48).

Much more critical are the integration constants of Ψ_r, C_1 and C_2. There is, unfortunately, no clear constraint that allows a straightforward determination. Somewhat more loosely, we can argue that the solution for $\Psi_r + \Psi_{\text{hom}}$ should match to the solution in the linear regime, $\Psi_\infty + \psi_{y0}$, at some point. In particular, let us consider the horseshoe region for $x = 0$. Thus, we consider the y-axis ($\theta = \pi/2$) and require that at a certain point $(x, y) = (0, y_c)$ $\Psi_{\text{hom}} + \psi(y_c) = \psi_{y0} + \Psi_\infty$:

$$-c_2 \frac{y_c^2}{m^2} + \Psi_r(y_c) = \psi_{y0}(y_c). \tag{58}$$

(Note that $\Psi_\infty = 0$ for $x = 0$ and $\cos 2\pi/2 = -1$.) In addition, it is required that the radial derivatives of the stream function match at this point:

$$-2c_2 \frac{y_c}{m^2} + (\partial_r \Psi_r)(y_c) = \partial_y \psi_{y0}(y_c). \tag{59}$$

Equation (59) will determine C_1, whereas equation (58) determines C_2. The integration constants follow straightforwardly from the Ψ_r and Ψ_r' expressions, although the very expressions are rather cumbersome. Assuming that $m \ll y_c \ll 1$ simplifies these significantly, however, and we may approximate:

$$C_1 \approx m y_c \left[\log\left(\frac{y_c}{\sqrt{2}}\right) + \gamma \right] \tag{60}$$

$$C_2 \approx C_1 \left(\frac{m}{y_c} + \gamma\right) + \log(y_c)(my_c - C_1) \tag{61}$$

$$+ \frac{1}{2} m \left[(-2 + 2\gamma - \log(2))y_c + \sqrt{2}\pi\right] + C_1 \log(m),$$

where γ is the Euler-Mascheroni constant.

The choice for the integration constants has now been rewritten in terms of y_c. Although there is no natural choice for y_c, it is expected that the hydrostatic assumption for ρ will become less accurate for larger r. Judging from Fig. 3, a typical scale will be $y \simeq 0.1$. Thus, y_c may represent the point where the nonlinear solution transfers to the linear solution of Section 3. Nevertheless, there is some freedom allowed in choosing the precise value of y_c. We find that with $y_c = 0.05$ the solution very well matches those of the numerical simulations and we stick to this value.

In summary, we have derived an analytical approximation of the perturbed flow pattern for a low mass planet ($m \ll 1$) under the assumptions that the density is radial, consistent with the isothermal EOS, $\Sigma = \exp(m/r)$, and that its solution reaches that of the unperturbed flow at $r \gg m$. The perturbed stream function is equation (42) with equation (51) for $\psi(r)$ and equation (48) for Ψ_{hom} with integration constants given by equations (54)–(60).

5.4 Synthetic streamline patterns

Figure 11 presents the streamline patterns derived from the analytical expressions presented above for the values of the mass parameter m. The free parameter y_c was fixed at 0.05. This figure can be compared to the middle panels of Fig. 9, the corresponding numerical solutions. The analytic solution retrieves most features very well. The analytical description is advantageous, because it is much faster than running a full numerical simulation and does not require interpolation of the result.

6 TRAJECTORIES OF SMALL PARTICLES AND THEIR ACCRETION BEHAVIOR

Having quantified the velocity structure around the planet in the form of the analytic solution presented in Section 5, trajectories of solid particles can be calculated. Particle trajectories will deviate from those of the gas (the streamlines)
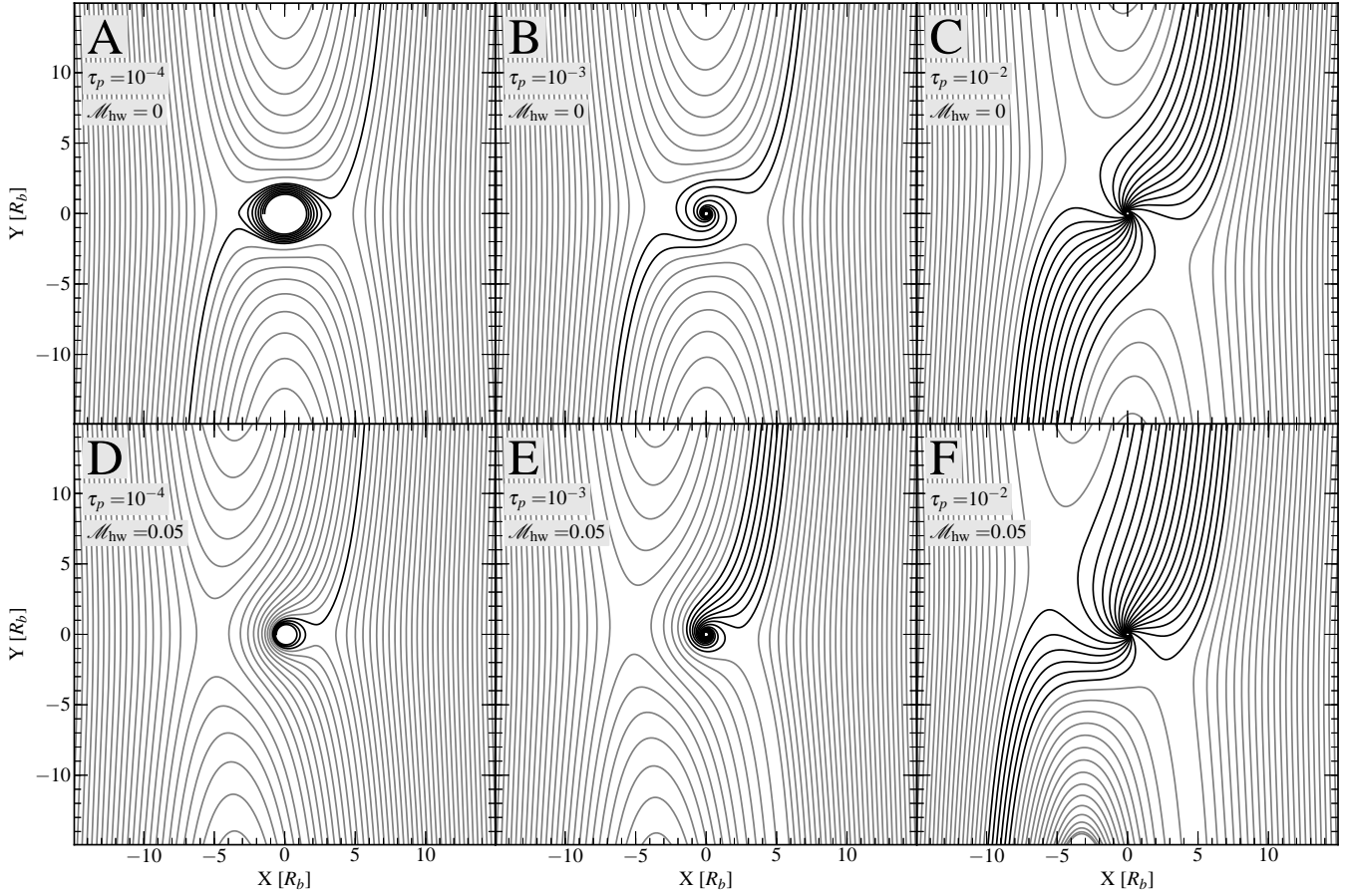
Figure 12. Trajectories of small, solid particles, characterized by their dimensionless friction time τ_p, in the vicinity of an $m = 10^{-2}$ planet. For $\tau_p \ll 1$, particles largely follow the streamlines of the gas. Trajectories that result in accretion by the protoplanet are highlighted black. Top panels: $\mathcal{M}_{hw} = 0$; bottom panels: $\mathcal{M}_{hw} = 0.05$.

due to their inertia. That is, it takes a solid particle a characteristic time – the friction or stopping time t_p – to align its motion with that of the gas. The dimensionless equivalent to t_p is $\tau_p = t_p \Omega_0$. Big particles ($\tau_p \gg 1$) like km-size planetesimals experience the gas only in the form of a small perturbation, which none the less is important to damp the random motions (eccentricity) of these bodies. Here, we consider small particles of $\tau_p \ll 1$. To first approximation, they tend to follow the gas. However, their not fully perfect coupling to the gas causes them to slowly settle due to the gravitational force, e.g., towards the central star (Weidenschilling 1977) or to planets (Ormel & Klahr 2010).

The particle size τ_p adds another dimension to the parameter space (along with m and $\mathcal{M}_{hw}$) and it is left to a follow-up work to conduct a full exploration. Figure 12 only presents a preview, where particle trajectories – *not* gas streamlines – are plotted for $m = 10^{-2}$, $\mathcal{M}_{hw} = 0$ and 0.05, and $\tau_p = 10^{-4}, 10^{-3}, 10^{-2}$. These correspond to small particles in the ~100 μm–10 mm size range, dependent on the values of the local gas density, disc radius, and particle internal density[4].

In Fig. 12 each curve represents a trajectory of a single particle. We have omitted drawing arrows to indicate their directions; but these are clear from comparison to Fig. 9b and e. Highlighted curves indicate particles that are accreted by the protoplanet. They all settle to the planet due to inspiraling motion in the prograde manner. This means that the accretion rate only depends on the mass of the planet, not on its radius. This accretion mechanism qualitatively differs from the way planetesimals are accreted, where one relies on a sufficiently close encounter to 'hit' the target. Accretion through settling may provide a very fast channel for growth. For $\tau_p \sim 1$ particles it has already been shown that their accretion radii are on the order of the Hill radius (Ormel & Klahr 2010; Lambrechts & Johansen 2012). However, for smaller particles accretion cross sections are likely smaller since they couple more strongly to the gas.

Indeed, Fig. 12a,d shows that the $\tau_p = 10^{-4}$ particles are difficult to accrete since their trajectories are strongly tied to the gas. The particle trajectories in these figures strongly resemble the gas streamlines of Fig. 9. In both

[4] The relation between the size s and friction time t_p depends on the gas drag law. In the Epstein regime (small particle, low gas density), $t_p = \rho_s s / \rho c_\infty$ where s is the particle size. When

particle sizes become larger than the mean-free-path l_{mfp} of the gas, t_p increases by a factor $\sim s/l_{mfp}$. For even larger particle sizes t_p starts to depend on the particle-gas velocity itself; but this regime is not considered here.

Fig. 12a,d only two particle streams penetrate the planet's atmosphere and settle slowly towards the center (at some point when it is clear that the particle will be accreted, the integration is stopped). Most particles that approach the planet, however, cannot break through the atmosphere as they, being strongly coupled to the gas, are dragged along gas streamlines.

Perets & Murray-Clay (2011) introduced the wind-shearing radius R_{ws} to quantify the competing effects of the (central) gravitational two body force and the gas drag force (which pulls particle away from accretion). That is, only particles with impact parameters less than R_{ws} can be accreted. A similar wind-shearing radius can be defined for low-mass planets surrounded by an atmosphere. First, it is noted that only particles near the atmosphere boundary will be accreted. Therefore, particles traveling along the Ψ_{atm} streamline are most likely to be accreted. The wind-shearing radius then becomes the bandwidth ΔR_{ws} over which the gravitational pull of the planet is sufficient to drag them into the atmosphere region. This idea will be explored further in a follow-up work.

Since the drag force equals $\mathbf{F} = (\mathbf{v}_p - \mathbf{v}_{gas})/t_p$, its influence will decrease with increasing friction time. For particles of friction time $\tau_p = 10^{-3}$ (the middle panels of Fig. 12) more particles accrete, but more so for the headwind case (7 counts) than the $\mathcal{M}_{hw} = 0$ case (4). Even for particle streams that do not accrete, deviations from the gas streamlines can be noted in Fig. 12b and e. For the $\tau_p = 10^{-2}$ particles in Fig. 12c and f the deviation from the streamlines is much more evident; close to the planet these particles decouple from the gas and the impact parameter for accretion is very large. Note finally that due to the prograde rotation of the gas in the atmosphere, small particles that enter the atmosphere will also start to rotate in a prograde manner; and once they have settled towards the central object they will convey this angular momentum to the accreting body, causing it to spin up. Small-particle accretion therefore naturally explains the observed preference for prograde spins of solar system bodies (Johansen & Lacerda 2010).

Obviously, Fig. 12 only presents a small subset of the parameter space and the above argumentation is rather qualitative. In a future work we will return to the question of the efficiency of small particle accretion and a provide a more quantitative analysis.

7 DISCUSSION

7.1 Caveats and extensions of the numerical method

We have described a method to compute the gas flow around gravitating bodies in steady state. The idea of the adopted approach is to solve for the stream function Ψ – a scalar quantity which fully describes the flow in 2D. The global flow pattern agrees well with previous numerical studies. However, the method employs several idealizations (the flow must be inviscid, 2D, barotropic, subsonic, etc), and it would be interesting to investigate whether these conditions can be relaxed. We remark that a supersonic expansion of the method has already been presented by Korycansky & Papaloizou (1996), which would allow us to explore particle accretion for more massive planets.

Since the focus of this work lies on embedded planets, an extension to three dimensions is perhaps the most obvious avenue. Indeed, 3D effects could have some effects, e.g., with regard to the width of the horseshoe region (Bate et al. 2003). Although the stream function formulation can be easily generalized to axisymmetric configurations (Lee & Stahler 2011), it is not commonly used for truly 3D geometries, like the shear flow consider in this work. But if we pursue this path, the 3D equivalent to equation (7) reads:

$$\Sigma\boldsymbol{v} = \nabla\Psi \times \nabla g, \tag{62}$$

where $g(\boldsymbol{x})$ is a second stream function. In 2D $g = z$ recovers equation (7). In 3D, constants of Ψ and g constitute surfaces, and the intersections of two surfaces defines a streamline. Following the procedure similar to Section 2 we can obtain a set of diffusion equations, one for each component of the vorticity. Unfortunately, the diffusion equations are now functions of two scalar quantities (Ψ and g) and therefore require a much more complex procedure to solve, probably involving an iterative approach.

7.2 Sensitivity to boundary conditions

A quite general, and somewhat surprising, feature of the numerical model is its sensitivity to the outer boundary constraints (BC). Here, we have used the linear solution presented in Section 3 to provide the flow velocity at the outer boundary. This turns out rather well, since the flow pattern is not very sensitive to the choice of r_{out}, although we found that the atmosphere region converges only for large r_{out} (requiring high numerical resolution). However, if the flow quantities at the outer boundary is changed to the background flow pattern, Ψ_∞, omitting ψ_{y0}–which means there is that $v_x = 0$ by construction – it is found that the flow pattern is very different. In some cases even retrograde rotation around the perturber is observed.

Since the linear solution that we presented in Fig. 4 agrees with previous works (e.g., Masset et al. 2006; Paardekooper & Papaloizou 2009), we have confidence in the robustness of the nonlinear calculations that we derived in the later sections. However, we have neglected possible contributions of the spiral density wave, i.e., from the Lindblad torque region. Paardekooper & Papaloizou (2009) considered the effect of the Lindblad torque (which originates at distances $x \gtrsim H$) on the flow in the vicinity of the protoplanet. They found that is was justified to neglect the Lindblad torque in the limit of zero softening of the gravitational potential (like in this work). Nevertheless, it is worthwhile to include the effects from the linear density wave theory (e.g., Ward 1997; Tanaka et al. 2002) as a boundary constraint, and to assess how this affects the flow structure near the planet.

7.3 Feasibility of the laminar approximation

The laminar approximation – and the neglect of turbulence – is another caveat. One stability criterion is the Richardson number, which measures the stability of a stratified flow:

$$\mathrm{Ri} = \frac{N^2}{(\partial v/\partial r)^2} = -\frac{g(r)}{\rho}\left(\frac{\partial\rho}{\partial r}\right) \bigg/ \left(\frac{\partial v_\theta}{\partial r}\right)^2 \tag{63}$$

where N^2 is the Brunt-Väisälä frequency. Richardson numbers below a critical value, $\mathrm{Ri_{crit}} \simeq 1/4$, indicate that the kinetic energy term due to shear will outweigh the (stabilizing) term due to density stratification. The flow then overturns and becomes unstable. We have calculated the Richardson number for the simulations presented in Fig. 9. In the far field ($r \gg 1$) it was found that $\mathrm{Ri} < \mathrm{Ri_{crit}}$; but this is due to our initial setup, where Σ_∞ is constant (allowing for gradients in Σ_∞ and other background quantities [$\tilde{w}_\infty$, c_∞] would be another obvious extension of the method.) However, Ri increases with decreasing r and closer to the planet $\mathrm{Ri} > \mathrm{Ri_{crit}}$.

Other instabilities may still operate though. For example, the flow within the atmosphere may be convectively unstable. Flow past bodies characterized by large Reynolds numbers will generally become turbulent in the wake of the body. Vortices may develop along the horseshoe streamline (Koller et al. 2003). Or the gas may be simply unstable to start with, e.g., due to the magneto-rotational instability (Balbus & Hawley 1991). All these effects render the laminar approximation rather fragile.

But it would be difficult, if not impossible, to present an analytic framework for non-steady flow. Our calculations provide the first order effect against which more specific simulations can be contrasted. For example, Fig. 12 shows the first-order effect of the interaction of particle with gas. Turbulence will change the particle trajectories; but, although their individual trajectories can be very different, it is yet to be shown that turbulent motions will result in a significant deviation to the *time-averaged* accretion rate.

7.4   Implications for protoplanet growth

Notwithstanding the canonical scenario (Safronov 1969), where protoplanetary cores are thought to be built up from big km-size (or larger) planetesimals, protoplanetary growth may in reality be driven by small particles, because:

(i) planetesimals will grind themselves down, before an embryo can accrete them (Kobayashi et al. 2010, 2011) or be trapped in resonances (and subsequently be ground down; Weidenschilling & Davis 1985).

(ii) (sub)mm-observations imply that a large reservoir of the dust is typically observed in the $\sim$mm/cm-size range (e.g., Andrews & Williams 2005).

(iii) growth by (big) planetesimals is slow. This is due to the negative feedback of a growing embryo on the planetesimal population (i.e., it excites them to large eccentricity, rendering growth less efficient; e.g., Kokubo & Ida 1998; Fortier et al. 2007).

For these reasons, it is relevant to study in greater detail the interaction between small particle and embryo. In a follow-up work we will perform a quantitative (parameter) study to obtain the accretion potential of small particles. However, from Fig. 12 two trends become clear. First, very small particles (i.e., dust) do not make formidable building blocks. They just follow the streamlines of the gas, and will only accrete on to the planet if the gas does not so as well. Secondly, accretion rates rise steeply with particle size. In a recent study, Lambrechts & Johansen (2012) showed that a putative core accretes $\tau_p \sim 0.1$ pebbles very rapidly with impact radii approaching the Hill radius, consistent with

the findings in Fig. 12c and f (the scale of the panels is the Hill radius). That this pebble accretion scenario results in high accretion rates is now widely recognized and may serve as an alternative to (the much slower) planetesimal accretion. However, one must not forget that $\tau_p = 1$ particle also *drift* the fastest (Weidenschilling 1977); they may be removed from the system before they encounter a protoplanet (Kobayashi et al. 2010). In this regard, somewhat smaller particles may offer a better channel for growth (see Ormel & Kobayashi 2012 for an assessment of the combined effects that affect the accretion behavior of small particles).

Protoplanets can also grow by contracting their atmospheres, allowing more gas to become bound. In this study this effect was crudely reflected by the transition density parameter Σ_T: the higher Σ_T the further the isothermal regime penetrates, and the more massive the atmosphere. More realistically, the atmosphere mass M_A is a function of the (solid and gas) opacity, accretion rate, equation of state, etc, and is obtained by solving the full equations of stellar structure (Mordasini et al. 2012). These calculations are usually carried out in 1D, assuming radial symmetry. But it is only through multidimensional (preferable 3D) studies that a true assessment of the *boundary* between the atmosphere and nebula gas can be obtained (e.g., Lissauer et al. 2009). In this work we find that the headwind plays a critical role. A headwind renders the flow – and therefore the atmosphere – asymmetrical, see e.g., Fig. 8c, which causes nebular material to penetrate the atmosphere within a fraction of the Bondi radius. The consequences of the asymmetry and, in particular, the small atmosphere radius have yet to be addressed by protoplanet atmosphere models. We remark that, although the importance of the asymmetry increases with increasing v_{hw}, it is a general feature – seen also at low headwinds.

8   SUMMARY AND CONCLUSIONS

In this manuscript the inviscid, steady state solution of a subsonic flow past gravitating bodies was considered. First, in Section 3, an approximate but analytic solution was presented. This solution only holds in the linear regime, that is, at distances much larger than the Bondi radius R_b. The linear solution served as a boundary condition for the full (nonlinear) numerical calculations (Section 4). These showed the importance of the atmosphere region (a nonlinear phenomenon), where the flow curls around the planet in the prograde direction. Using the findings from the numerical simulations, we next constructed a more complete analytical approximation of the flow pattern, which captures the dynamics of the atmosphere region (Section 5). This solution very well matches the numerical findings and may be used in subsequent studies for which the flow pattern at scales of R_b is important.

The adopted framework is quite general, with parameters describing the mass of the perturber, the headwind velocity v_{hw}, and the shear parameter ω_∞. Apart from Section 4.3, this study has focused on the flow pattern past small planets embedded in Keplerian discs ($w_\infty = -3\Omega_0/2$). However, flow patterns around 'bodies' occur in diverse astrophysical settings, e.g., in (small) satellites embedded circumplanetary disks (e.g., Estrada et al. 2009), star forma-

tion (Krumholz et al. 2005), or accretion disks around black holes (McKernan et al. 2011). As long as these embedded objects do not open gaps and the system is in steady-state, the framework constructed in this paper also provides a description for the flow pattern in these environments.

The key findings of this study are the following:

(i) For flows without shear, the steady-state flow pattern resembles that of an hourglass (Fig. 5), where gravity focuses the streamlines.

(ii) For Keplerian shear flows the vorticity, which is amplified near the planet due to conservation of vortensity, plays the dominant role. There is a point in the simulation where the flow stagnates. In general there are two solutions for the associated stagnation streamline – one defining the atmosphere region and one defining the horseshoe region – which only coincide when $v_{\mathrm{hw}} = 0$.

(iii) For the (general) $v_{\mathrm{hw}} \neq 0$ case, the boundary of the atmosphere is asymmetric and lies within the Bondi sphere (Fig. 10). The size of the atmosphere reduces with increasing headwind but its averaged radius is best approximated by the Bondi radius R_b (rather than the Hill radius).

(iv) When the flow is subsonic (in particularly, $v_{\mathrm{hw}} \ll 1$), the density near the Bondi radius can be well approximated by the hydrostatic solution, such that Σ becomes a function of radius only. In this approximation, an analytic solution for the stream function has been obtained (see Section 5 and Appendix B). This solution can be used to compute the gas drag force which solid particles experience during their encounter with the planet.

(v) When they can penetrate the atmosphere region, particles can be accreted as they settle to the planet through the circumplanetary disc. Accretion of small particles (dust) is suppressed as they strongly couple to the gas flow, but we find that for ∼mm-size and larger particles accretion rates should be high. There is also tentative evidence that a (moderate) headwind accelerates particle sweepup, due to the smaller atmosphere.

REFERENCES

Adachi I., Hayashi C., Nakazawa K., 1976, Progress of Theoretical Physics, 56, 1756
Andrews S. M., Williams J. P., 2005, ApJ, 631, 1134
Balbus S. A., Hawley J. F., 1991, ApJ, 376, 214
Bate M. R., Lubow S. H., Ogilvie G. I., Miller K. A., 2003, MNRAS, 341, 213
Bondi H., Hoyle F., 1944, MNRAS, 104, 273
Bonnell I. A., Bate M. R., Clarke C. J., Pringle J. E., 2001, MNRAS, 323, 785
D'Angelo G., Henning T., Kley W., 2002, A&A, 385, 647
Dong R., Rafikov R. R., Stone J. M., Petrovich C., 2011, ApJ, 741, 56
Estrada P. R., Mosqueira I., Lissauer J. J., D'Angelo G., Cruikshank D. P., 2009, Formation of Jupiter and Conditions for Accretion of the Galilean Satellites. p. 27
Fortier A., Benvenuto O. G., Brunini A., 2007, A&A, 473, 311
Goldreich P., Tremaine S., 1980, ApJ, 241, 425
Guyer J. E., Wheeler D., Warren J. A., 2009, Computing in Science & Engineering, 11, 6
Hori Y., Ikoma M., 2010, ApJ, 714, 1343
Hoyle F., Lyttleton R. A., 1939, Proceedings of the Cambridge Philosophical Society, 35, 405
Hubickyj O., Bodenheimer P., Lissauer J. J., 2005, Icarus, 179, 415
Hunt R., 1979, MNRAS, 188, 83
Ikoma M., Genda H., 2006, ApJ, 648, 696
Ikoma M., Hori Y., 2012, ApJ, 753, 66
Inaba S., Ikoma M., 2003, A&A, 410, 711
Johansen A., Lacerda P., 2010, MNRAS, 404, 475
Kley W., Shankar A., Burkert A., 1995, A&A, 297, 739
Kobayashi H., Tanaka H., Krivov A. V., 2011, ApJ, 738, 35
Kobayashi H., Tanaka H., Krivov A. V., Inaba S., 2010, Icarus, 209, 836
Kokubo E., Ida S., 1998, Icarus, 131, 171
Koller J., Li H., Lin D. N. C., 2003, ApJ, 596, L91
Korycansky D. G., Papaloizou J. C. B., 1996, ApJ, 105, 181
Krumholz M. R., McKee C. F., Klein R. I., 2005, ApJ, 618, 757
Lambrechts M., Johansen A., 2012, A&A, 544, A32
Landau L. D., Lifshitz E. M., 1959, Fluid mechanics
Lee A. T., Stahler S. W., 2011, MNRAS, 416, 3177
Lissauer J. J., Hubickyj O., D'Angelo G., Bodenheimer P., 2009, Icarus, 199, 338
Lopez E. D., Fortney J. J., Miller N. K., 2012, ArXiv e-prints:1205.0010
Machida M. N., Kokubo E., Inutsuka S.-I., Matsumoto T., 2010, MNRAS, 405, 1227
Masset F. S., D'Angelo G., Kley W., 2006, ApJ, 652, 730
McKernan B., Ford K. E. S., Lyra W., Perets H. B., Winter L. M., Yaqoob T., 2011, MNRAS, 417, L103
Miki S., 1982, Progress of Theoretical Physics, 67, 1053
Mizuno H., 1980, Progress of Theoretical Physics, 64, 544
Morbidelli A., Nesvorny D., 2012, ArXiv e-prints:1208.4687
Mordasini C., Alibert Y., Klahr H., Henning T., 2012, ArXiv e-prints:1206.6103
Müller T. W. A., Kley W., Meru F., 2012, A&A, 541, A123
Muto T., Inutsuka S., 2009, ApJ, 695, 1132
Nelson A. F., Benz W., 2003, ApJ, 589, 578
Ormel C. W., Klahr H. H., 2010, A&A, 520, A43
Ormel C. W., Kobayashi H., 2012, ApJ, 747, 115
Paardekooper S., 2007, A&A, 462, 355
Paardekooper S.-J., 2009, A&A, 506, L9

Paardekooper S.-J., Papaloizou J. C. B., 2009, MNRAS, 394, 2297

Perets H. B., Murray-Clay R. A., 2011, ApJ, 733, 56

Pollack J. B., Hubickyj O., Bodenheimer P., Lissauer J. J., Podolak M., Greenzweig Y., 1996, Icarus, 124, 62

Rafikov R. R., 2006, ApJ, 648, 666

Ruffert M., 1995, A&AS, 113, 133

Safronov V. S., 1969, Evolution of the Protoplanetary Cloud and Formation of Earth and the Planets. Moscow: Nauka. Transl. 1972 NASA Tech. F-677

Shima E., Matsuda T., Takeda H., Sawada K., 1985, MNRAS, 217, 367

Stevenson D. J., 1982, Planet. Space Sci., 30, 755

Tanaka H., Takeuchi T., Ward W. R., 2002, ApJ, 565, 1257

Tanigawa T., Ohtsuki K., Machida M. N., 2012, ApJ, 747, 47

Terquem C., Heinemann T., 2011, MNRAS, 418, 1928

Ward W. R., 1986, Icarus, 67, 164

Ward W. R., 1991, in Lunar and Planetary Institute Science Conference Abstracts Vol. 22 of Lunar and Planetary Institute Science Conference Abstracts, Horsehoe Orbit Drag. p. 1463

Ward W. R., 1997, Icarus, 126, 261

Weidenschilling S. J., 1977, MNRAS, 180, 57

Weidenschilling S. J., 1997, Icarus, 127, 290

Weidenschilling S. J., Davis D. R., 1985, Icarus, 62, 16

Wuchterl G., 1993, Icarus, 106, 323

APPENDIX A: DERIVATION OF EQUATIONS (29), (30)

The linearization of equation (25) proceeds as follows. The term $\nabla\Psi/\Sigma$ is replaced by $\nabla(\Psi_\infty + \psi)/(1+\sigma) \approx \nabla\psi + (1-\sigma)\nabla\Psi_\infty$, where it is assumed that $\sigma \ll 1$ and that we can neglect terms like $\sigma\nabla\psi$. Since $\nabla\Psi_\infty = (-\omega_\infty x + \mathcal{M}_{\rm hw})\mathbf{e}_x$ only has an x-component, the divergence operator $\nabla\cdot$ is replaced by a differential ∂_x. In this way equation (29) becomes

$$\nabla^2\psi - (\partial_x\sigma)(\omega_\infty x - \mathcal{M}_{\rm hw}) - \omega_\infty(1-\sigma) = -\omega_\infty - \tilde{\omega}\sigma. \quad (A1)$$

from which, after re-arranging, equation (29) is retrieved.

For the linearization of equation (26), an isothermal EOS is assumed, such that $W(\Sigma) = \log\Sigma \approx \sigma$. The kinetic term $|\nabla\Psi|^2/2\Sigma$ is linearized as

$$\frac{(\nabla\Psi_\infty + \nabla\psi)^2}{2(1+\sigma)^2} \approx \frac{1}{2}|\nabla\Psi_\infty|^2 - \sigma|\nabla\Psi_\infty|^2 + \nabla\Psi_\infty\cdot\nabla\psi$$

$$= \frac{1}{2}|\nabla\Psi_\infty|^2 + (\mathcal{M}_{\rm hw} - \omega_\infty x)(\partial_x\psi) - \sigma(\mathcal{M}_{\rm hw} - \omega_\infty x)^2 \quad (A2)$$

On the RHS of equation (26) $\Psi = \Psi_\infty + \psi$. After noting that the first order terms cancel (they obey the far-field solution), equation (30) is obtained.

APPENDIX B: FULL, NONLINEAR EXPRESSIONS FOR THE FLOW PATTERN

In Section 5 an approximate solution for the flow in terms of the stream function (see equation 7) was presented in terms of an homogeneous solution, $\Psi_{\rm hom}$, and a particular

solution, $\Psi(r)$: $\Psi(r,\theta) = \Psi_{\rm hom}(r,\theta) + \Psi(r)$. We found that (equation 49):

$$\Psi'(r) = \frac{e^{\frac{m}{r}}\left[m^2\tilde{\omega}\text{Ei}\left(\frac{m}{r}\right) - \tilde{\omega}r(m+r)e^{\frac{m}{r}} + 2(r^2 + C_1)\right]}{2r}, \quad (B1)$$

where C_1 is an integration constant, and $\text{Ei}(x)$ the exponential integral

$$\text{Ei}(x) = \int_{-\infty}^{x} dt\,\frac{e^t}{t}. \quad (B2)$$

Equation (B1) can be integrated once more

$$\Psi_r(r) = \frac{1}{4}\left[-\text{Ei}\left(\frac{m}{r}\right)\left(4C_1 + m^2\tilde{\omega}\text{Ei}\left(\frac{m}{r}\right) + 2m^2\right)\right.$$

$$+ 4C_2 + 8m^2\tilde{\omega}\text{Ei}\left(\frac{2m}{r}\right)$$

$$\left. + re^{m/r}\left(2(m+r) - \tilde{\omega}e^{m/r}(4m+r)\right)\right] \quad (B3)$$

These expressions contain two integration constant, C_1 and C_2. As argued in Section 5, these are chosen such that they match the linear solution at a point $(x,y) = (0, y_c)$ or $r = y_c$ and $\theta = \pi/2$ in radial coordinates. This resulted in conditions given by equations (58), (59). The derivative of equation (33), ψ_{y0} reads

$$\partial_y\psi_{y0} = m\left[\cos\tilde{y}\,\text{Ci}(\tilde{y}) - \frac{1}{2}\sin\tilde{y}\left(\pi - 2\,\text{Si}(\tilde{y})\right)\right], \quad (B4)$$

where $\tilde{y} = y/\sqrt{2}$, and $y > 0$ and a Keplerian disk ($\tilde{\omega} = 1/2$) have been assumed.

The constants C_1, C_2 follow by rearranging equations (58), (59), i.e., by isolating C_1 and C_2. This is a straightforward procedure, but rather cumbersome. For a Keplerian disk ($\tilde{\omega} = 1/2$) we obtain in this way

$$C_1 = e^{-\frac{m}{y_c}}\left\{my_c\,\text{Ci}(\tilde{y_c})\cos\tilde{y_c} - e^{\frac{m}{y_c}}\left[\frac{1}{4}m^2\text{Ei}\left(\frac{m}{y_c}\right) + y_c^2\right]\right.$$

$$- my_c\left[\frac{\pi}{2} - \text{Si}(\tilde{y_c})\right]\sin\tilde{y_c}$$

$$\left. + \frac{1}{4}y_c e^{\frac{2m}{y_c}}(y_c + m) + \frac{1}{4}y_c(3y_c + m)\right\}. \quad (B5)$$

An expression for C_2 can be obtained in a similar way. In the limit of $m \ll y_c \ll 1$ these expressions simplify significantly and read:

$$C_1 \approx my_c\left(\log\left(\frac{y_c}{\sqrt{2}}\right) + \gamma\right) \quad (B6)$$

$$C_2 \approx \frac{1}{24}m\left\{12\sqrt{2}\pi + 4y_c\left[\log\left(\frac{y_c^6}{8}\right) + 6\gamma - 6\right.\right. \quad (B7)$$

$$\left.\left. + \left(\log\left(\frac{y_c^6}{8}\right) + 6\gamma\right)\left(-\log(y_c) + \log(m) + \gamma\right)\right]\right\}$$

where $\gamma \approx 0.577$ is the Euler-Mascheroni constant.

To conclude, let us summarize the expressions for the flow velocity that follow from the full nonlinear model. For the radial component it reads:

$$v_r = \frac{1}{\Sigma}\frac{\partial_\theta\Psi}{r} = \frac{1}{\Sigma r}\partial_\theta\Psi_{\rm hom}, \quad (B8)$$

where $\Sigma = \exp(m/r)$, and $\Psi_{\rm hom}$ is given by equation (48)

which includes the c_1, c_2 integration constants. The azimuthal flow velocity reads

$$v_\theta = -\frac{1}{\Sigma}\partial_r\Psi = -\frac{1}{\Sigma}\left[\partial_r\Psi_{\mathrm{hom}} + \Psi'(r)\right] \qquad (\mathrm{B}9)$$

and includes in addition the integration constant C_1 through the Ψ'_r term (equation B1).

This paper has been typeset from a T_EX/ L^AT_EX file prepared by the author.